Aerospace Science and Technology 126 (2022) 107625

Contents lists available at ScienceDirect

Aerospace Science and Technology

www.elsevier.com/locate/aescte

Review

Numerical-experimental evaluation and modelling of aerodynamic ground effect for small-scale tilted propellers at low Reynolds numbers

Ambar Garofano-Soldado [a,*], Pedro J. Sanchez-Cuevas [a,b], Guillermo Heredia [a], Anibal Ollero [a]

[a] GRVC Robotics Lab Seville, University of Seville, Spain
[b] Space Robotics Research Group, SnT, University of Luxembourg, Luxembourg

ARTICLE INFO

Article history:
Received 1 February 2022
Received in revised form 25 April 2022
Accepted 7 May 2022
Available online 11 May 2022
Communicated by Damiano Casalino

Keywords:
Aerodynamic Effect
Aerial Robot
UAV
CFD
Propeller

ABSTRACT

In recent years, aerial manipulators with fully-actuated capabilities are gaining popularity for being used in aerial manipulation operations such as critical infrastructure inspection or aerial manipulation tasks. Those scenarios usually demand the aerial platform to operate in constrained and narrow scenarios. It is well known that in these situations, the interaction of the wake generated by the propellers with the environment can significantly alter and change the performance of the rotors. Most studies have addressed this problem by considering the ground effect in hover conditions or during the landing maneuver for co-planar multirotor. However, few works analyze the behaviour of tilted rotors, which are used in fully actuated multirotor configurations thanks to their omnidirectional motion capabilities. This paper presents a numerical-experimental evaluation of the aerodynamic ground effect for small-scale tilted propellers at low Reynolds numbers. This aerodynamic effect has been experimentally evaluated through an extensive testing campaign in a testbench designed for this purpose which has been complemented by a CFD-based study. CFD results have been validated through a mesh independence study and a CFD-experimental propeller performance comparison. A numerical model has been also proposed to capture the dependence of thrust with distance to the ground and angle of inclination between the propeller and ground planes. We demonstrate that the proximity to the ground of tilted rotors decreases the thrust increment due to the ground effect as the tilt angle (θ) increases. This means that Cheeseman's classical theory is inapplicable, as it only considers the distance from the ground without reference to how the thrust increment changes with the tilt angle. This outcome enables future aerial robotic applications that strongly demand accurate aerodynamic effect models to operate close to obstacles and narrow environments.

1. Introduction

Unmanned Aerial Vehicles (UAVs) and Micro Air Vehicles (MAVs) are significantly increasing their application range [1]. Typically, these aerial robots have been used as flying sensors to perform perceptual tasks such as remote surveillance and reconnaissance [2,3], visual inspection of large infrastructures [4,5] or filming activities [6,7]. However, emerging applications such as package delivery [8], contact inspections [9,10], warehouse inventory [11] and, in general, aerial robotic manipulation operations [12] require these rotorcrafts to fly close to obstacles and objects or within narrow environments. Propellers operating near obstacles experience different aerodynamic effects. This constrains the free development of the rotor wake and disturbs the propeller performance [13].

The ground effect on helicopters has been studied since the 1930s [14] to characterise the hovering aerodynamic performance [15]. In 1937, Betz [14] proposed a theoretical model based on replacing the helicopter rotor by a sink and applying the method of images. Knight et al. [16] considered two cylindrical vortex sheets located at a distance of $2z$ of equal strength and opposite direction. In 1947, Zbrozek [17] analysed the ground effect experimentally. Later, Cheeseman and Bennett [18] found that the flow pattern of a rotor in the vicinity of the ground was better matched with a source. Thus, [18] used blade element theory and the method of images to model the increase in thrust experienced by a rotor operating close to the ground under different conditions. Cheeseman and Bennett's model is typically used because it allows results to be obtained with high accuracy compared to experimental evidence for large propellers such as helicopters or MAVs. In addition,

* Corresponding author.
E-mail address: agarofano@us.es (A. Garofano-Soldado).

https://doi.org/10.1016/j.ast.2022.107625

Nomenclature

θ	Tilt angle of the propeller relative to the ground	deg
z	Ground distance from propeller hub	m
α	Angle of attack of a blade	deg
β	Blade pitch angle	deg
ϕ	Inflow angle	deg
U	Resultant velocity of a blade section	m/s
U_T	Tangential component of velocity in a blade section	m/s
U_P	Normal component of velocity in a blade section	m/s
Re	Reynolds number	
ρ	Air density	kg/m^3
μ	Air dynamic viscosity	kg/ms
V_ω	Rotational velocity	m/s
Ω	Angular velocity	rad/s
$R_{75\%}$	Propeller radius at 3/4 of the centre of rotation	m
$c_{75\%}$	Propeller chord at 3/4 of the centre of rotation	m
F_x, F_y, F_z	Sensor force components	N
T_x, T_y, T_z	Sensor torque components	Nm
X_A, Y_A, Z_A	Axes in the absolute reference frame	m
X_B, Y_B, Z_B	Axes in the propeller reference frame	m
C_T	Propeller thrust coefficient	
C_{T_x}	Horizontal component of the thrust coefficient	
C_{T_z}	Vertical component of the thrust coefficient	
C_Q	Propeller torque coefficient	
R	Propeller radius	m
D	Propeller diameter	m
A	Rotor disk area	m^2
T	Propeller thrust	N
Q	Propeller torque	Nm
T_{IGE}	Thrust In-Ground-Effect	N
T_{OGE}	Thrust Out-of-Ground-Effect	N
v_{IGE}	Induced velocity in ground effect	m/s
$v_{i\infty}$	Induced velocity without ground effect	m/s
δv_i	Induced velocity on the rotor caused by the image rotor	m/s
V_h	Hover induced velocity	m/s
$f_c(\theta)$	Target function	
a_0, a_1, b_1	Coefficients proposed for the ground effect model	
β_j	Model coefficients calculated with the gradient descent algorithm	
$J(\beta_j)$	Cost function	
$h_\beta(z^i, \theta^i)$	Hypothesis function	
y^i	Thrust ratio T_{IGE}/T_{OGE}	
s	Number of samples	
γ	Learning rate	

Acronyms

CFD	Computational Fluid Dynamics
ESC	Electronic Stability Control
IGE	In-Ground-Effect
$MAVs$	Micro Air Vehicles
MRF	Multiple Reference Frame
OGE	Out-of-Ground Effect
$RANS$	Reynolds Average Navier-Stokes
SST	Shear Stress Transport
$UAVs$	Unmanned Aerial Vehicles
BET	Blade Element Theory

the formulation of this model is relatively simple and depends only on the radius of the rotor (R) and the distance between the propeller and the ground plane (z). Other operating conditions, such as forward flight, were considered [18–20]. Since the first experimental tests by Zbrozek [17], some ground effect models have been derived from experimental evidence. Hayden (1976) [21] proposed an empirical model to analyse the ground effect in hover, which overpredicts the Cheeseman and Bennett model. Then, Curtis [22] presented the aerodynamic performance of a helicopter rotor when positioned close to the ground for low advance ratios. Other authors have focused on examining the rotor wake when it is constrained by the presence of the ground plane [23–27].

In the last decade, particular attention has been devoted to exploring the aerodynamic interactions of multirotor [28–32] and small scale rotors [33,34]. There is a need for in-depth knowledge of the behaviour of UAVs when approaching certain surfaces. In this way, proximity effects can be counteracted by incorporating a controller adapted to absorb aerodynamic disturbances [20,35,36]. In addition, the feasibility of tilting the propellers of a multirotor to perform tasks requiring direct contact between the aerial platform and the environment has been investigated. In [37], a new design of a fully actuated hexarotor with tilting propellers was presented and the application of control techniques to aid platform stabilisation. Other work has been carried out along the same lines [38], [39]. The aerodynamic effects of tilted rotors are not considered in these control laws as there is no thorough understanding of how the forces on a rotor change with inclination and distance from the ground. For instance, unlike co-planar aerial manipulators that classically accomplish the manipulation operation while they are hovering (and necessarily horizontal), a fully actuated aerial robot can perform a hover-flight while tilting with respect to the horizontal plane. This presents a completely new casuistry. According to [28], the disturbance that affects a co-planar multirotor is generating a “safe” behaviour cause it is always generating stabilization pitch and roll torques. However, due to fully-actuated robots usually have tilted propellers and can maintain an inclined hover, the aerodynamic ground effect will disturb the 6DoF, including the yaw axis. This situation will significantly impact the stability of these aerial robots, their safety, and the definition of their control allocation matrix. Moreover, a fully-actuated aerial manipulator will be affected by this effect mainly when flying close to an obstacle and specifically, when accomplishing the manipulation operation. The manipulation operation is usually when the accuracy and precision needed are higher. This means that any disturbance should be considered to guarantee the success and safety conditions during the operation.

Though extensive previous works have characterised the aerodynamic performance of large and small-scale rotors parallel to the ground, there is little work on tilted rotors with respect to the ground or co-planar rotors operating at inclined surfaces. However, recent advances in aerial manipulation present the fully-actuated multirotor as the optimal candidate for certain contact-based operations [40]. These multirotor have full pose (position and orientation) tracking capabilities. Also, could land or hover very close to the ground or a different obstacle, maintaining a desired angle with the ground. In 1960, Fradenburgh [41] was the first to study the variation of the thrust ratio of a helicopter and annular jet considering the aerodynamic ground effect with different angles and heights above ground. Xin [42] proposed an extension of the inflow model for rotors at different heights above an inclined ground in hovering conditions. Different ground inclinations were analysed. The results were compared with the free-vortex/panel model. They also found that an asymmetry in the rotor wake appeared with the ground angle. More recent contributions were reported in [43],

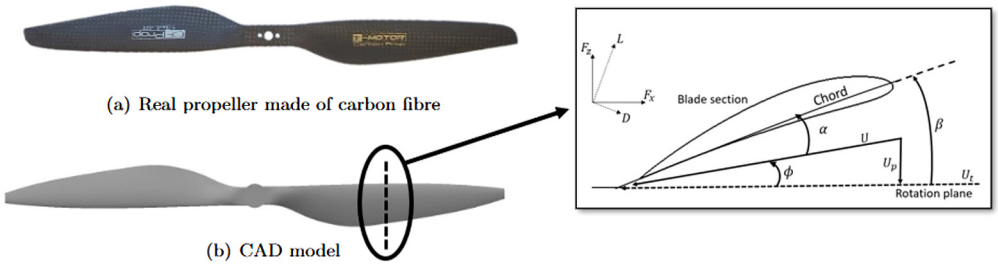

Fig. 1. Real and geometric model of the T-Motor propeller - $13'' \times 4.4''$.

[44]. Platzer et al. examined the flow field of a rotor in the neighbourhood of an inclined surface using particle image velocimetry (PIV) and unsteady numerical simulations. Then, Pasquali et al. [45] used experimental and numerical techniques to analyse the evolution of the rotor wake on an inclined and parallel ground. The bounded domain method and method of images were employed and compared. However, there are no detailed studies showing the thrust augmentation of a small-scale rotor with tilt angle and distance to a parallel surface. Accordingly, neither theoretical nor empirical thrust models taking into account inclination have been developed.

Due to the continuous development of computational fluid dynamics (CFD) tools, various simulation methods have been considered in the past to evaluate the influence of the ground on a rotor [43,46], [47–49]. Computational Fluid Dynamics is a handy tool for reproducing fluid behaviour around a propeller. Although several simulation techniques exist [50], Reynolds Averaged Navier-Stokes (RANS) models are less expensive and are used to estimate time-averaged parameters. In recent years, the number of investigations on propeller performance analysis with RANS models has increased [46–49,51–58] both high and low Reynolds numbers. Their suitability with experimental sets has been proven in several works [52,55,58]. Based on previous work, RANS models are considered capable of solving the proposed problem and will be used throughout this analysis. In this regard, the Multiple Reference Frame (MRF) method will be used to solve the 3D propeller flows. MRF has been adopted to examine flows around propellers by other authors both in free [51–54] and constrained environment [56,59]. Nevertheless, the adequacy of the MRF method has not been proved for inclined propellers, where the flow patterns are different from the co-planar case.

In general, this study describes the ground effect of tilted rotors using small-scale propellers operating at low Reynolds numbers. So far, no ground effect model has been presented under these conditions. Considering the growth in the field of UAVs, it is necessary to analyse and quantify the effects that may appear when certain tasks are performed. In summary, the contributions of this research are listed as follows:

- Investigation of the influence of inclination of rotor (θ) and distance to the ground (z) to quantify the thrust increase. The findings have been benchmarked against models developed in the past, highlighting the need to include the angle θ in the ground effect analysis. Indeed, the parameter θ has not been accounted for in small-scale propellers until the current study.
- A comprehensive 3D stationary CFD simulation-based study with a wide range of Reynolds numbers ($[0.46 - 2.2] \cdot 10^5$) and propeller diameters from 9 to 18 inches. Moreover, rotor inclinations of up to about 40° and various ground clearances have been assumed.
- Evaluation of a CFD-based methodology for flow simulation around propellers in confined environments. In particular, the MRF method has been applied. Although its reliability has been demonstrated for rotors parallel to the ground (see [59]), the fluid behaviour is distinct if the rotor is tilted. MRF has been verified with data from the propeller manufacturer in free environments and then with the experimental setup under IGE and OGE conditions. A method with a low computational cost that allows obtaining adequate results in even less time than the time required for bench testing.
- Proposal of first ground effect model with tilted rotors in small-scale propellers is presented to capture the dependence on both tilt angle (θ) and ground distance (z). It has been derived a CFD simulation data-driven model using the gradient descent algorithm. For this purpose, a modification to the classical Cheeseman and Bennett theory has been made, where the first harmonic of the inflow models has been considered. The applicability of the proposed model has also been assessed.

The remainder of the paper is organized as follows. Section 2 details the geometry of the different propellers used throughout this study, the Reynolds number range, the experimental setup and the fundamentals of Computational Fluid Dynamics (CFD). The computational domain, the boundary conditions, and the turbulent model are introduced. Section 3 shows the validation of the CFD methodology. On the one hand, a grid independence study is presented. On the other hand, the propeller performance achieved by the proposed CFD methodology is evaluated with the manufacturer's data. Section 4 is devoted to presenting the ground effect results obtained from both the experimental setup and numerical simulations. The feasibility of the CFD method is discussed. Then, the flow field visualization is illustrated to understand the change in rotor performance with tilt. In Section 5, a data-driven ground effect model with tilted rotors is proposed and validated for several propellers. Section 6 discusses the applications and limitations of the proposed model. Finally, it draws the conclusions from the ground effect analysis and gives ideas for future work along the same lines.

2. Materials and methods

2.1. Propeller geometry

The first propeller selected is a small-scale T-Motor propeller with a diameter of 13 inches and a pitch of 4.4 inches. Fig. 1(a) and Fig. 1(b) present both the carbon fibre propeller used in the experimental study and the 3D geometry of the propeller employed in the numerical analysis respectively. Fig. 1 also shows a detail of the geometry of a blade section according to the blade element theory (BET). Here, the angle of attack is defined as $\alpha = \beta - \phi$, where β is the pitch angle of the cross-section and ϕ is the inflow angle, defined as $\phi = tan^{-1}(U_p/U_T)$. U is the resultant velocity and depends on the normal (U_p) and tangential (U_T) component to the plane of rotation. In the current study, freestream velocity is not taken into account as a result the velocity U_p will depend only on the induced velocities through the disk rotor. Moreover, the evolu-

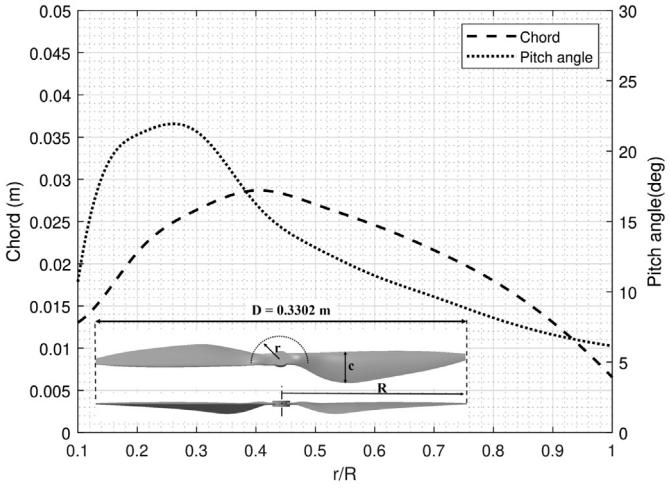

Fig. 2. Geometry, chord and twist angle distribution of the T-Motor propeller - 13″ × 4.4″ used in experimental-numerical analysis.

tion of the chord and the pitch angle of the propeller is shown in Fig. 2.

Two extra propellers have been used to validate the proposed model and evaluate its applicability. These propellers are APC 9x4.4" and one T-Motor propeller 18x6.1" (see Fig. 3), the 3D geometrical model, the dimensions and chord and twist angle distributions of these propellers are shown.

2.2. Reynolds number range

This section presents the range of Reynolds numbers evaluated in this work. It is known that in order to model the flow behaviour around a propeller, the Reynolds number, based on the rotational speed and the chord at 3/4 of the radius location, plays an important role. The performance of a propeller will change with the Reynolds number, as shown in previous studies [60]. Also, the Reynolds number in small-scale propellers will be much lower than in large-scale propellers used in helicopters. The Reynolds number when freestream velocity is not taken into account can be defined as follows [61]:

$$Re_{75\%} = \frac{\rho V_\omega c_{75\%}}{\mu} \tag{1}$$

where the air density is ρ = 1.225 kg/m^3, the dynamic viscosity is $\mu = 1.7894 \cdot 10^{-5}$ kg/ms, the rotational velocity is $V_\omega = \Omega R_{75\%}$, Ω is the angular velocity, $R_{75\%}$ and $c_{75\%}$ is the radius and chord of the propeller located at 3/4 centre of rotation, respectively. In this study, propellers are operating at low Reynolds numbers since the maximum value is $2.2 \cdot 10^5$ [62]. It is well known that low Reynolds numbers are related to bubble separation, which is caused by adverse pressure gradients. For low advance ratios, a large number of cross-sections of the blade are in a stall condition. However, Coriolis effects, based on the rotation and the radial component of the velocity, delay the separation of the boundary layer and consequently the stall [63].

Table 1 defines the Reynolds number of each propeller considered in this study.

2.3. Experimental setup

Fig. 4 shows the customized test bench used during the experiments in GRVC's facilities. It is made up of an aluminum structure of 1m x 1m x 1m where an Axia80-M20 force/torque sensor has been mounted. This sensor allows measuring the six components

Table 1
Reynolds Number for different propellers considered in this study.

Propeller	Reynold number
APC 9x4.4	$(0.46, 0.74) \cdot 10^5$
T-Motor 13x4.4	$(0.88, 1.1) \cdot 10^5$
T-Motor 18x6.1	$(1.5, 2.2) \cdot 10^5$

of force and torque with a resolution of $1/10N$ and $1/200Nm$, respectively. The sensing range is 500N for the forces F_x, F_y, 900N for F_z and $20Nm$ for T_x, T_y and T_z and the sensor frequency is 2 kHz.

An Arduino Mega 2560 is used to control the motor. The motor PWM input is sent from the computer to achieve a speed of 6300 revolutions per minute (rpm). Rotation speed is measured with an external tachometer during the experiments. The operating range of the motors used in multirotor is between 50% − 60% throttle. The selected speed is within this range and is a typical value for the motor and propeller chosen in this analysis. Last, two $360W$ parallel power supplies have been used to power the sensor and the motor to maintain constant voltage conditions in all the experiments.

A total of 40 experiments has been carried out. Fig. 5 shows the two parameters considered to evaluate the aerodynamic ground effect. Unlike classical ground effect analysis where only the ground distance was taken into account [28,30,32,56], this study also considers the relative angle between the ground and the propeller (θ). In each experiment, five different measurements have been taken in order to take the mean value. The standard deviation of the force was calculated for each distance (z) and angle (θ), reaching a maximum value of $0.087N$ and a minimum value of $0.002N$. These results show that the sensor is highly accurate.

The data collection process takes 85 seconds for each test. At first, the motor is switched off for 15 seconds. Then, the propeller is rotating at a constant speed for 10 seconds. Finally, the motor speed is reduced to a minimum speed for 60 seconds to avoid an increase in motor temperature before a new test was done. All experimental data have been collected in the absolute reference frame S_A, defined by the axes X_A, Y_A, Z_A. In addition, the body frame S_B = X_B, Y_B, Z_B is defined, which can be obtained by rotating the absolute reference frame S_A.

2.4. CFD settings

Computational fluid dynamics methods are typically used to analyze propeller performance and understand vortex generation mechanisms. For that, the finite volume method is used where the Reynolds Averaged Navier-Stokes (RANS) equations are solved on an unstructured mesh. The incompressible flow simplification is performed.

According to the literature [51–55,59,64], there are two main CFD techniques to simulate of rotating flows: the multiple reference frame (MRF) and the sliding mesh methods. MRF is a steady-state approach. It divides the domain into several zones: a stationary zone, where the equations will be applied in a stationary frame, and a zone assigned to a rotational velocity relative to the propeller axis. These zones lead to the appearance of an interface that allows information to be exchanged between the stationary zone and the rotational zone. In contrast to other authors [49], this analysis considers the classical multi-zone MRF method. On the contrary, the sliding mesh method considers the propeller's motion at each time-step and provides a time-dependent solution. The computational domain is defined similarly to the MRF method. In many cases, the output of the MRF method is taken, in fact, as the initial condition for the sliding mesh method. While the appli-

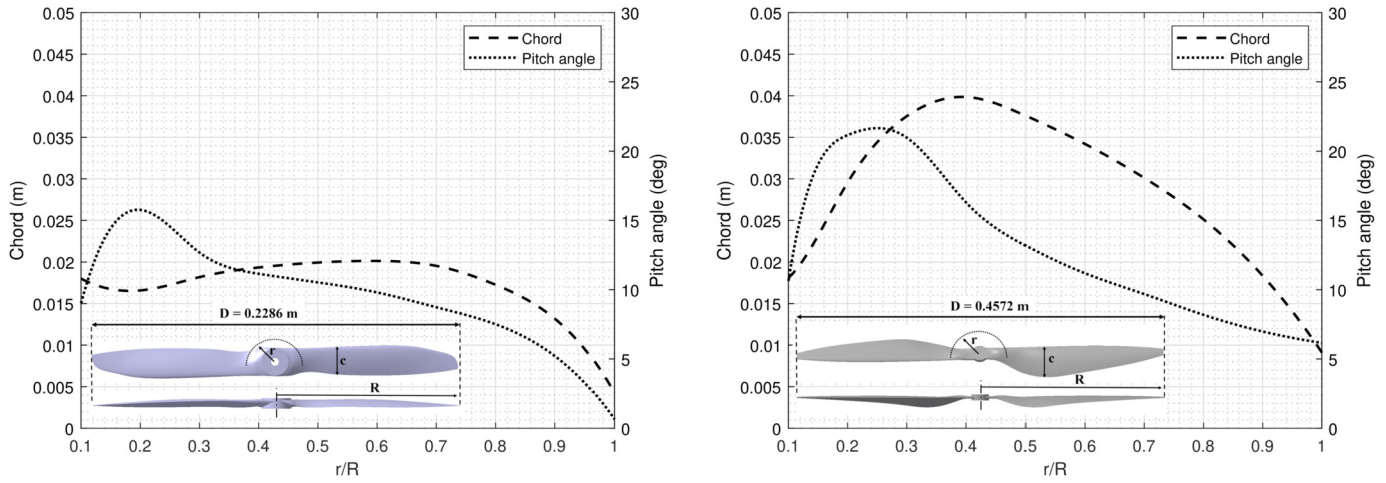

Fig. 3. Geometry, chord and twist angle distribution of the propellers used to validate the proposed ground effect model. Left) APC propeller - 9″ × 4.4″ used to validate the proposed ground effect model. Right) T-Motor propeller - 18″ × 6.1″.

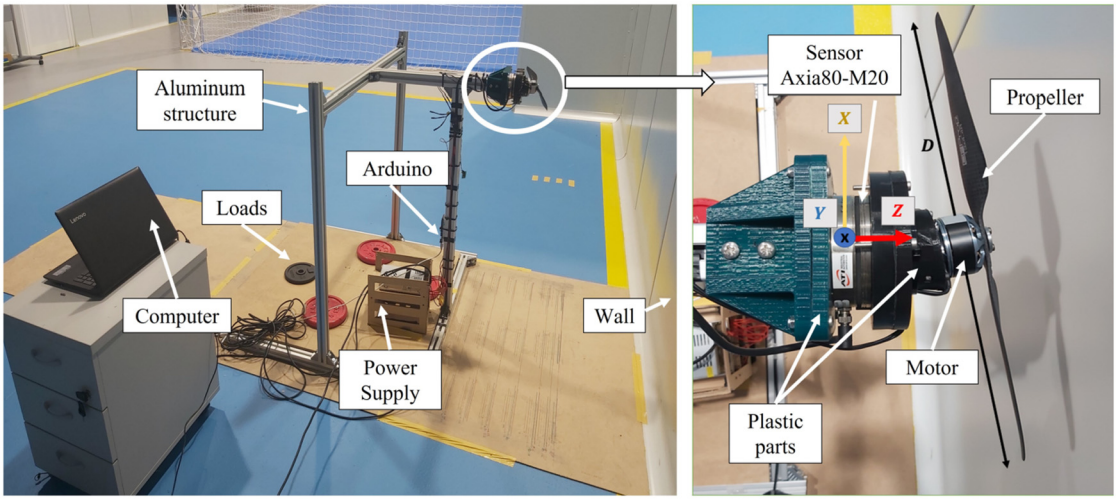

Fig. 4. Test bench designed at Robotic, Vision, and Control Group (GRVC) to study ground effect with single tilted rotors. The structure is moved to locate the propeller's centre of rotation at different distances from the wall (z). The inclination of the motor (θ) is achieved by using inclined printed plastic parts.

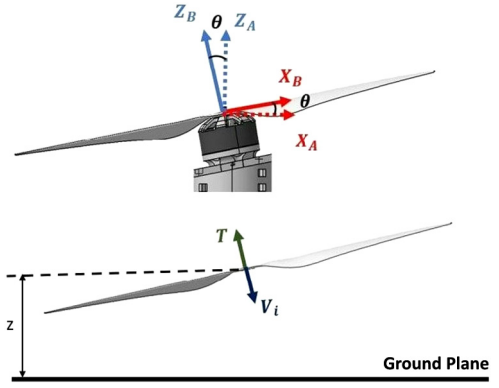

Fig. 5. Absolute reference frame X_A, Y_A, Z_A and reference frame on blade axes X_B, Y_B, Z_B of the propeller and variables tested in the ground effect investigation.

cation of transient techniques usually produces better results, the computational effort is prohibitively high.

This paper uses MFR due to its simplicity, fastness, and fair accuracy. This method allows for analyse of the fluid flow around a propeller when it is close to the ground without the presence of external disturbances. In the past, other authors have analyzed the small and large scale propeller performance with this method in both free and confined environments [48,49,51,53,56]. However, as a tilted propeller approaches the ground, the interaction of the rotor wake with the ground surface causes an asymmetric pattern that becomes more noticeable as the tilt increases [42]. As a consequence, it is necessary to ensure that this stationary approach (MRF) allows modelling the flow behaviour to obtain the small-scale propeller performance. Silva et al. show how the MRF method is able to predict the wake breakdown and ring vortex using unstructured meshes. However, under IGE conditions, it is a challenge to capture these vortical structures accurately [49].

Fig. 6 shows the computational domain set up to simulate the ground effect with a tilted propeller. It has three different domains. An external stationary domain with a diameter of $20R$, a cylindrical inner domain with a diameter of $5R$, and a rotating domain to enclose the propeller. The inner domain allows a mesh transition in order to capture the fluid flow behaviour accurately. In this domain, a flow with a rotational speed of $6300RPM$ is induced. The rotational domain and the propeller are rotated at an angle θ with respect to the ground. The vertical distance from the centre of rotation of the propeller to the ground plane is defined as z. The dimensions of the inner and outer domains change for each z value. Therefore, a parametric analysis has been performed where

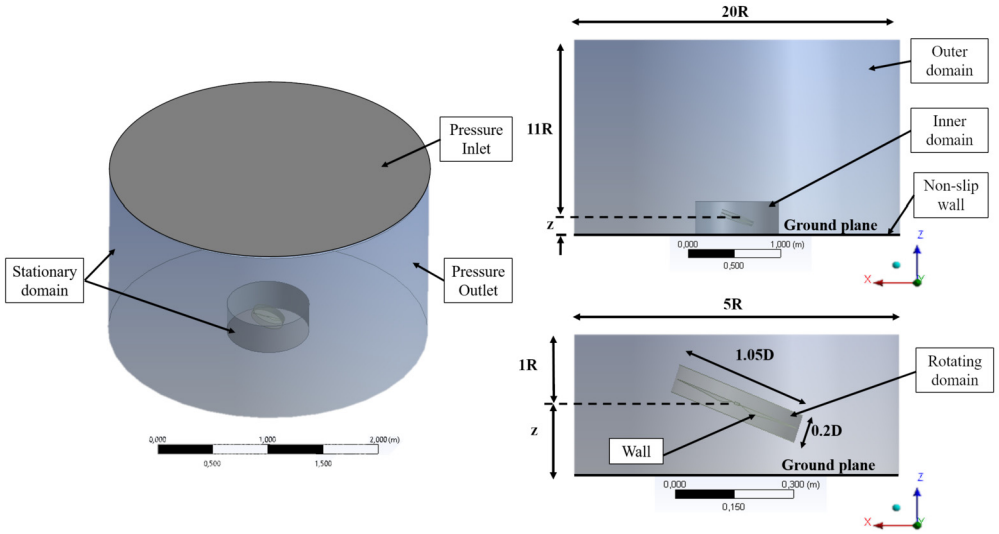

Fig. 6. Computational domain specified to analyse the ground effect on tilted rotors. The propeller is placed at a height z = 1R with respect to the ground. The boundary condition adopted to evaluate the aerodynamic performance is given.

the parameters θ and z are changed. This will generate a specific geometry and mesh for each configuration.

The commercial software ANSYS-Fluent has been used for the calculations. The pressure-based coupled algorithm is used to solve the momentum and the pressure-based continuity equations. The coupled algorithm significantly reduces the number of iterations required to converge. However, the computational time is increased compared with a segregated algorithm, where each variable is solved sequentially. Green-Gauss Node-Based Gradient is employed to discretise the diffusive and convective terms of the conservation equation. The second-order scheme is chosen for Turbulent Kinetic Energy (k), Specific Dissipation Rate (ω), and pressure interpolation. The turbulence model used to solve the problem is the shear stress transport (SST) $k-\omega$ turbulence model proposed by Menter [65]. It combines the $k-\epsilon$ model in the remote region from the wall and the $k-\omega$ model in the near-wall region using blending functions. This is defined with two equations, one for the Turbulent Kinetic Energy (k) and one for the Specific Dissipation Rate (ω). Due to the Reynolds number range (see section 2.2) in which turbulent flows are found, it is considered that the SST k-w model should be applied [52]. The SST $k-\omega$ turbulence model has been used by other authors to analyze the aerodynamic performance of small-scale propellers [53–55,57,58,66]. Moreover, the simulations results were compared with experimental data obtaining a satisfactory agreement [52,55,58]. The turbulent intensity is set as 0.1%. This value has been achieved by taking measurements in an empty wind tunnel for all operating conditions [60,67]. Logarithmic wall functions are used to solve the boundary layer. In recent work, this approach has been considered in the near-wall region [52]. Additionally, a full ground effect case with a 20 degree inclination has been simulated with the Realizable k-e turbulence model. This turbulence model was used by [48] to analyse the stability of an aerial platform close to the ground plane. The differences found between the two turbulence models are negligible. However, the computational time and the instability of the solution with the Realizable $k-\epsilon$ model are increasing.

Fig. 6 shows the boundary conditions. In the upper boundary, the inlet is defined as a pressure inlet where the total gauge pressure is set to 0 Pa. The outlet is set in the lateral boundary of the cylindrical domain as a pressure outlet with gauge pressure 0 Pa. The ground plane and the propeller are defined as non-slip walls. Between the rotational and stationary domains, interfaces are generated that allow the separation of the two domains. An absolute velocity formulation has been used in this analysis, i.e. the equations are solved in each sub-domain. Therefore, no transformation is needed at the interface.

This numerical analysis is divided into two parts: first, the simulation results will be compared with the experimental results to validate the defined CFD model. Thus, the angles analysed by simulation will be: 0°, 10°, 20° and 30° and dimensionless heights $z/R =$ 0.6, 0.75, 1, 1.5, 1.5, 2, 2.5, 3, 3.5, 4, 5. Second, when it is verified that the CFD model accurately fits the experimental results, this model will be extended to obtain results for other tilt angles such as 5°, 15°, 25°, 35° and 40°. For angles greater than 25°, it has not been possible to obtain results for heights less than z = 0.75R as the cylindrical rotational domain intersects with the ground plane. A total of 87 simulations has been carried out to characterise the aerodynamics ground effect with tilted rotors.

3. CFD validation

3.1. Mesh evaluation

A mesh independence study was conducted to ensure that the solution does not depend on the mesh size. This process allows defining a mesh with enough quality to achieve reliable and accurate results, minimise computational time and achieve good convergence of the solution. In this analysis, four different meshes have been created where the cell size located on the surface of the propeller, the cell size of the propeller leading edge and the sizes of interfaces have increased from mesh 1 to mesh 4. Additionally, automatic mesh refinement is applied. Fig. 7 shows the four defined grids in the rotational domain and Table 2 shows the number of nodes and elements in each of the domains and interfaces generated. As can be seen, Mesh 1 and 2 are coarser with 1.06 y 2.2 million elements respectively, while Mesh 3 and 4 are finer with 3.3 and 4.8 million respectively. In all cases, unstructured meshes were made with a refinement in the leading edge of the propeller and in the wake region. This study was carried out for a 20 degree tilt angle and for a height $z = 1R$. In order to evaluate the accuracy of each mesh, the results of the thrust and torque coefficient of the propeller were calculated according to:

$$C_T = \frac{T}{\rho A \Omega^2 R^2} \tag{2}$$

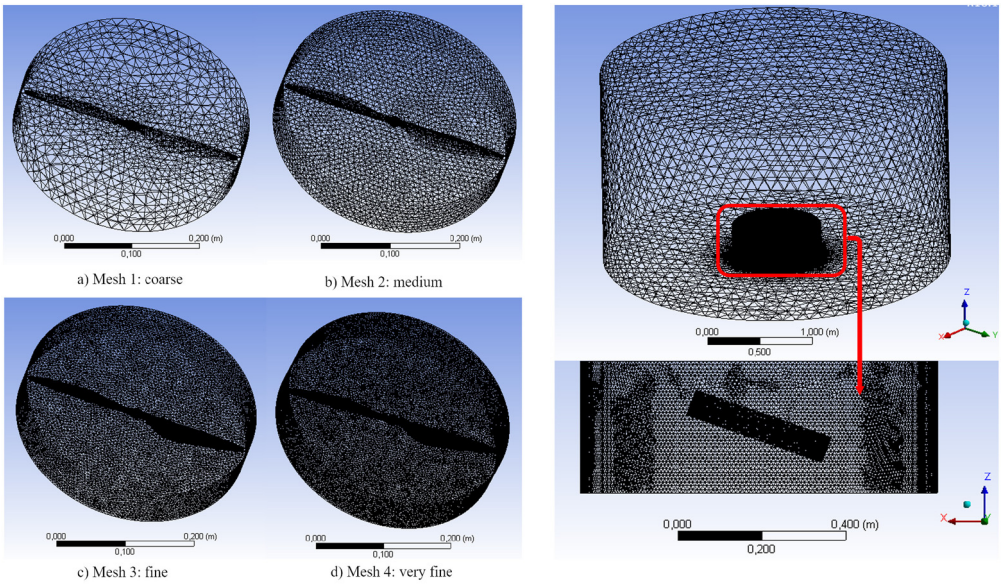

Fig. 7. On the left-hand side, definition of four different meshes (Mesh 1: coarse, Mesh 2: medium, Mesh 3: fine, Mesh 4: very fine) of the rotational domain. On the right-hand side, mesh chosen for the complete computational domain.

Table 2
Number of elements and nodes in the stationary, rotational domain and at the interface separating the two zones for meshes 1 (coarse), 2 (medium), 3 (fine) and 4 (very fine).

Mesh densities		Rotating domain	Stationary domain	Interfaces	Total
Mesh 1	Nodes	13.210	171.549	2.848	184.759
	Elements	70.166	993.442	12.396	1.063.608
Mesh 2	Nodes	30.653	354.682	27.288	385.335
	Elements	163.357	2.076.988	136.696	2.240.345
Mesh 3	Nodes	202.980	385.787	80.416	588.767
	Elements	1.110.512	2.243.860	414.278	3.354.372
Mesh 4	Nodes	440.121	418.441	133.352	858.562
	Elements	2.409.443	2.421.935	694.222	4.831.378

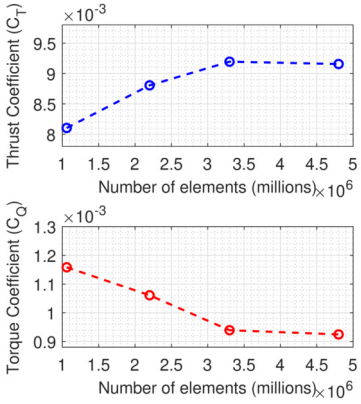

Fig. 8. Thrust and moment coefficient versus number of elements (in millions) for each of the meshes proposed in the mesh independence study. They show the convergence of the solution as the mesh is refined.

$$C_Q = \frac{Q}{\rho A \Omega^2 R^3} \tag{3}$$

where ρ is the air density, A is the rotor disk area (m^2), Ω is the angular speed (revolutions per minute), T is the thrust of the propeller (N), and Q is the torque of the propeller (Nm). As can be seen in Fig. 8, from 3.3 million elements onward, the results barely vary. Between mesh 1 and mesh 3, the thrust coefficient changes by 11.63% and torque coefficient by 18.18%, while between mesh 3 and mesh 4 the variation of both coefficients is minimum, being 0.4% for C_T and 1.7% for C_Q. For this reason, mesh 3 is the best option as it allows obtaining accurate results with lower computational costs than what would be achieved with meshes close to 5 million elements. Table 3 lists the size of the selected element of mesh 3 at the propeller, blade edge, and computational domain interfaces. The mesh of the selected computational domain is shown on the right side of Fig. 7. In all cases, the mesh quality parameters have been evaluated, obtaining orthogonal quality values above 0.15 [55]. To ensure convergence of the solution, the simulations iterate until the change in propeller thrust is less than 0.01% in the last 1000 iterations, where the residual errors found are smaller than 10^{-6}. Meshes similar to those proposed in this work are created by [52]. The average wall y+ value in mesh 3 is about 31. This value is similar to the one used in [57,68]. Although the full advantages of the turbulence model are not being taken advantage of, greater stability and convergence of the solution is achieved than if other models were used. On the contrary,

Table 3
Element size defined in the propeller and interfaces of computational domain for mesh 3, which is the best choice after grid independence analysis.

Zone	Element size (m)
Propeller	0.001
Interfaces	0.005
Edge blade	0.0003

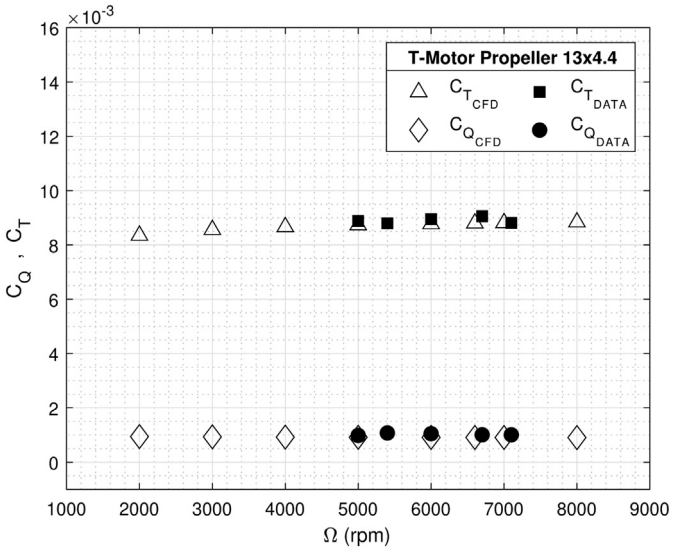

Fig. 9. Static performance of the T-Motor 13x4.4 propeller for different rotational speeds (rpm): comparison of thrust and torque coefficients (C_T and C_Q) between CFD results and manufacturer's data. Propeller used in experimental-numerical analysis.

the flow separation is not accurately predicted. The minimum element size related to the wall value is $1 \cdot 10^{-4} m$.

3.2. Propeller performance comparison

A total of 22 simulations has been carried out to validate our CFD results. These simulations have assessed the static performance of the three propellers considered in this study (see section 2.1) with seven rotational speeds. Each simulation was performed in a free environment. The static performance results have been compared with the data provided by the manufacturer T-Motor and APC [69,70].

Figs. 9 and 10 show the variation of thrust and torque coefficient with rotational speed (rpm) resulting from both CFD simulations and manufacturer's data. These coefficients have been obtained by applying Eq. (2) and Eq. (3). It is observed that when the rotational speed (and as a consequence the Reynolds number) increases, the thrust coefficient increases while the torque coefficient remains practically constant. Regarding the thrust coefficient, it is noted that the CFD results overestimate the data found in [69,70] for the T-Motor 18x6.1 and APC 9x4.4 propellers. In contrast, the CFD torque coefficient is underestimated in all cases. However, the C_T and C_Q errors of the three propellers examined are less than 5% and 10%, respectively. Under static conditions, the fidelity of a rotor's performance is related to the ability to capture the vortex structures of the blade tip [51]. Based on the results presented in this section, it is established that the CFD model is adequate to capture the forces on the propeller in a free environment. Also, it is assumed that the tip flow structures can be predicted although not as rigorously as in higher-order schemes.

4. Ground effect for small-scale tilted propellers

4.1. Experimental evaluation of the CFD-based method

This section compares experimental and simulation results according to the procedures described in section 2.3 and section 2.4 respectively. In both procedures, the co-planar configuration, where the rotor is parallel to the ground (θ = 0°), and three tilt angles (θ = 10°, 20° and 30°) have been analysed. Furthermore, ten distances measured from the centre of rotation of the propeller to the wall (z/R = 0.6, 0.75, 1, 1.5, 2, 2.5, 3, 3.5, 4, 5) were assessed.

Fig. 11 shows the horizontal and vertical components of the thrust coefficient (C_{T_x} and C_{T_z}) versus dimensionless ground distance (z/R) for each rotor tilt angle (θ). The experimental results are shown in dotted lines and the CFD results in dashed lines. In addition, the triangular marker indicates the vertical component of the force, and the circular marker the horizontal component. It can be seen that the thrust coefficient of the rotor increases as it approaches the ground in all cases. However, as the angle of inclination increases, the vertical component of the force reduces and the horizontal component becomes larger. The numerical results overpredict the trend of the thrust coefficient curve compared to the experimental curves for all angles. An offset is observed between the simulation and experimental results for each of the configurations analysed. This offset remains practically constant from height $1.5R$ onwards. However, the discrepancies between simulated and experimental results are considered acceptable taking into account the errors arising from both methods of data collection. In Table 4 the root mean square error (RMSE) between the simulation and experimental results of C_{T_z}, C_{T_x} are shown.

To investigate the ground effect, the thrust ratio T_{IGE}/T_{OGE} is typically used, where T_{IGE} is the thrust In-Ground-Effect and T_{OGE} is thrust Out-of-Ground-Effect. This ratio gives the percentage increase in thrust experienced by the rotor when the ground is close. Accordingly, in Fig. 12, the thrust ratio of the experimental and simulation data is plotted versus the dimensionless distance z/R. Nevertheless, Fig. 11 has been presented to give an estimate of how each of the force components varies.

For the case of a rotor parallel to the ground ($\theta = 0°$) the results are compared with Cheeseman and Bennett's classical helicopter theory [18]:

$$\frac{T_{IGE}}{T_{OGE}} = \frac{1}{1 - \left(\frac{R}{4z}\right)^2} \tag{4}$$

The results show that the ground effect is negligible when z/R is approximately greater than 2.5. For angles 0°, 10° and 20°, the closest distance to the wall is $0.6R$. In these cases, the thrust is increased by 13.3%, 9.6% and 8.7%, respectively. For the 30° angle, the minimum distance at which simulations have been performed is $0.75R$, since the rotational domain interfered with the ground plane for smaller distances. For this height, the thrust increases experienced by the rotor for angles 0°, 10°, 20° and 30° would be 10.4%, 7.8%, 6.1% and 5%, respectively. The CFD results fit quite accurately to those obtained by experimentation, reaching a maximum error of 5.1% for a height of $0.6R$ and a tilt of 10°.

Regarding the observed discrepancies, they can be attributed to both numerical and experimental errors. On the experimental side, there are several sources of errors that could generate this kind of discrepancy. For instance, although the experiments were carried out thoroughly, the positioning parallel to the wall of the structure in Fig. 4 is done manually. This could introduce errors if at some distance z it is not completely parallel. The ESC used to control the rpms of the rotor is a COTS ESC. In most cases, those control and regulate the speed of the electric motor by closing the control loop at the current measurement level. This means that the value of rpm could be not exactly the same as the one we have imposed in the simulations. The power supply used during the experiment is also a low-price system that could be sensitive to some environmental changes like the temperature [51]. Moreover, considering that the propeller is placed close to the plastic parts and sensor, this could create an extra interference with the flow field. However, it has been verified that there is no interference of the test bench on the propeller. For this purpose, after

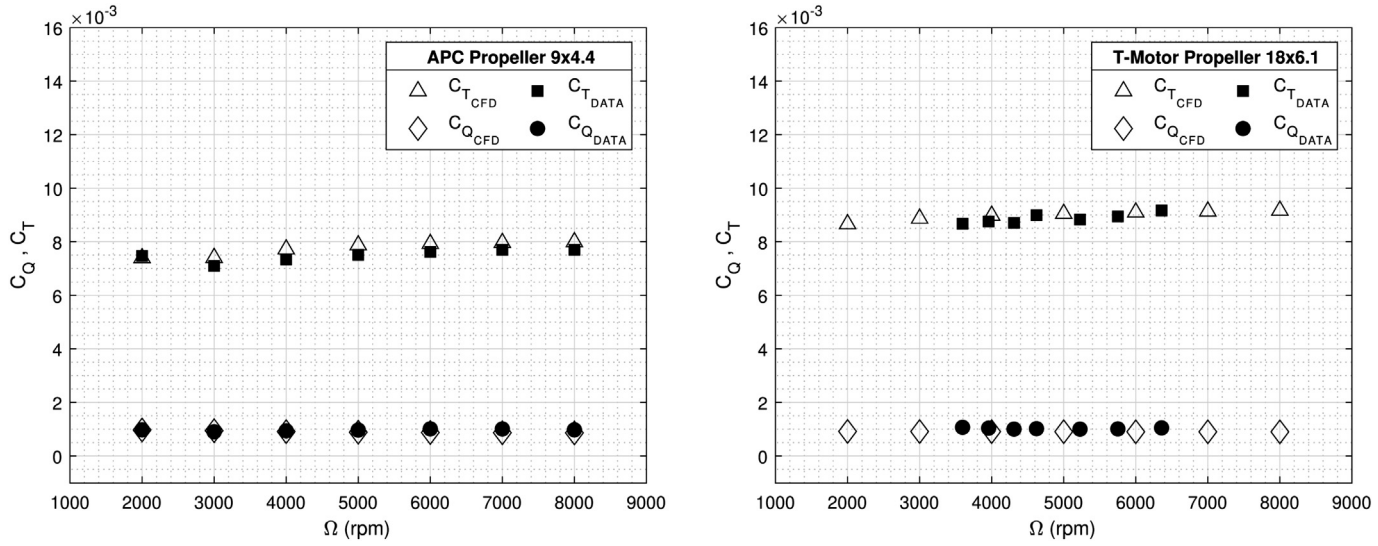

Fig. 10. Static performance of the T-Motor 18x6.1 and APC 9x4.4 propellers for different rotational speeds (rpm): comparison of thrust and torque coefficients (C_T and C_Q) between CFD results and manufacturer's data. Propellers used to validate the proposed ground effect model.

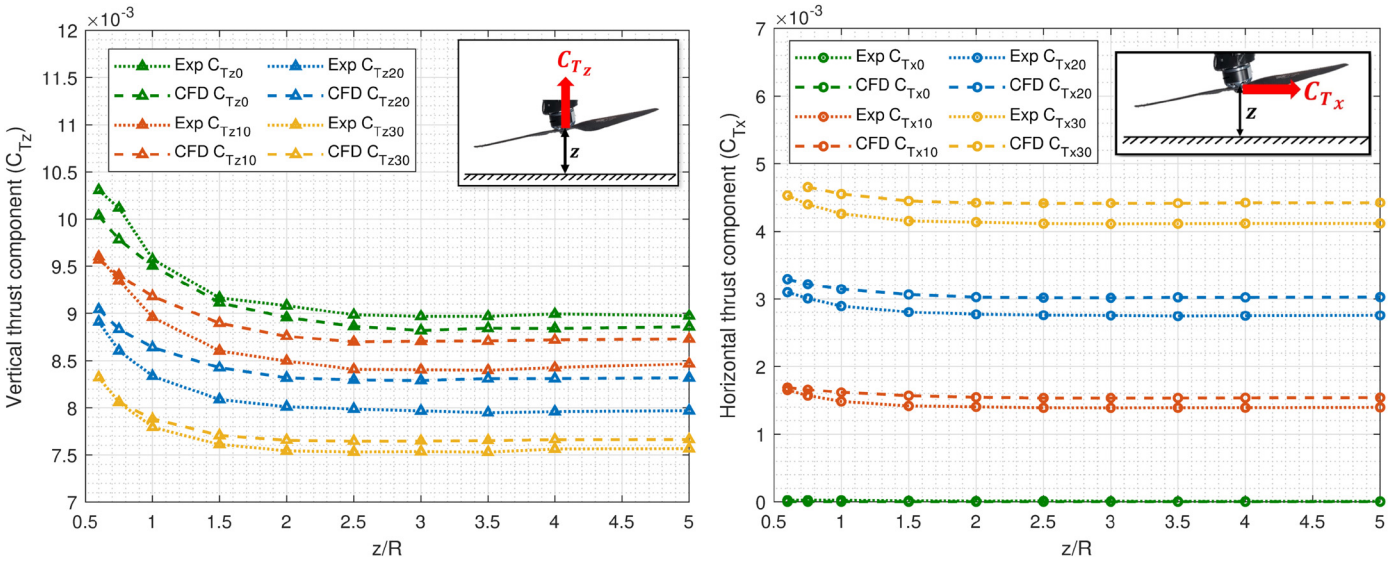

Fig. 11. Vertical and horizontal component of the thrust coefficient versus z/R dimensionless distance for angles 0°, 10°, 20° and 30° derived by experiment and CFD simulations.

Table 4
RMSE of the proposed CFD methodology for vertical and horizontal component of the thrust coefficient considering angles 0°, 10°, 20° and 30°.

Angle	Coefficients	0.6	0.75	1	1.5	2	2.5	3	3.5	4	5
0°	C_{T_x}	7.27e-06	7.25e-06	6.63e-06	4.37e-06	2.90e-06	3.30e-06	2.31e-06	1.27e-06	1.70e-06	1.40e-06
	C_{T_z}	8.56e-05	9.49e-05	2.25e-05	1.58e-05	4.04e-05	3.84e-05	4.68e-05	3.92e-05	4.83e-05	3.60e-05
10°	C_{T_x}	1.30e-05	2.82e-05	4.25e-05	4.76e-05	4.35e-05	4.49e-05	4.53e-05	4.51e-05	4.52e-05	4.45e-05
	C_{T_z}	1.3e-04	8.03e-05	5.18e-06	3.68e-05	2.29e-05	2.54e-05	3.27e-05	3.20e-05	2.46e-05	2.82e-05
20°	C_{T_x}	6.13e-05	6.60e-05	7.86e-05	8.22e-05	8.05e-05	8.20e-05	8.29e-05	8.81e-05	8.63e-05	8.57e-05
	C_{T_z}	4.17e-05	7.25e-05	9.60e-05	1.07e-4	9.68e-05	9.73e-05	1.02e-04	1.14e-04	1.11e-04	1.10e-04
30°	C_{T_x}	-	8.52e-05	9.82e-05	9.91e-05	9.49e-05	1e-04	1.02e-04	1e-04	1e-04	1.02e-04
	C_{T_z}	-	2.95e-07	2.94e-05	3.23e-05	3.82e-05	3.88e-05	3.81e-05	4.15e-05	3.38e-05	3.30e-05

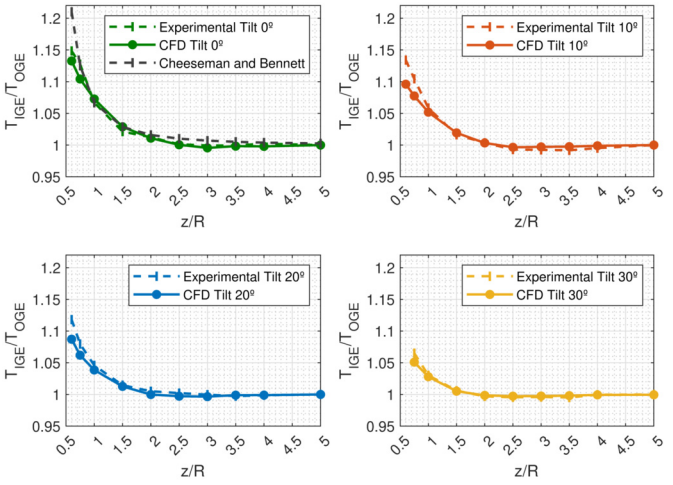

Fig. 12. Comparison of experimental and simulated thrust ratio T_{IGE}/T_{OGE} for angles 0°, 10°, 20°, and 30° assuming ten different distances from the ground. The co-planar case is contrasted with the Cheeseman and Bennett theory.

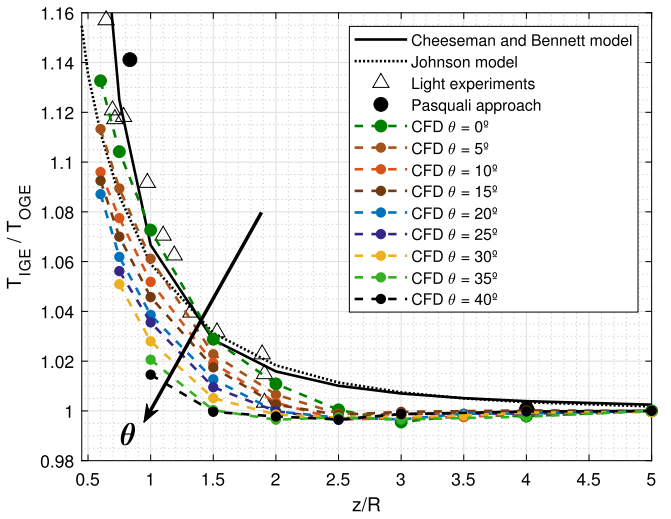

Fig. 13. CFD results of the thrust increase experienced by a propeller inclined at angles 0°, 5°, 10°, 15°, 20°, 25°, 30°, 35°, and 40° versus non-dimensional distance z/R.

validating the CFD model presented in section 2.4, six additional simulations have been performed to quantify the change in thrust force with and without structure. Thus, the same structure presented in Fig. 4 has been introduced in CFD. Thrust force errors of less than 0.3% have been found for the distances closer to the wall (0.6R, 0.75R and 1R) and 1% for the distances farther away (2R, 3R and 5R). Therefore, it is considered that the setup interference on the propeller is negligible. It is true that it is impossible to repeat exactly the same conditions in simulation and in the real world, even though, we assume this is not a critical drawback due to dimensionless values correcting these minor deviations according to Fig. 12.

Apart from these, in the simulation side, the main differences could be arising as a result of using a stationary approximation. MRF, also known as the "frozen approach", is a simplified model that does not consider transient effects and flow unsteadiness. Indeed, the offset observed in Fig. 11 is attributed to the simplifications of the numerical model. In [52], this trend is also observed when comparing experimental wind tunnel results with those obtained with the FR model. However, in our case, the errors do not exceed 5% for C_{T_z} and 8% for C_{T_x}, while in [52], the errors are around 20%. This shows the reliability of the developed test bench. In any case, it should be highlighted that after dimensioning, the offset disappears and has no influence on the ground effect results. Fig. 12 shows that the most significant errors occur in the areas closest to the ground. Even so, the error does not reach 1% in the worst case. This demonstrates that the defined CFD model in section 2.4 is good enough to rigorously predict the behaviour of the flow when it is close to a surface.

Experimental tests take longer to run than simulation tests, as each inclined piece has to be designed, manufactured, and assembled on the structure. Furthermore, the structure has to be positioned at ten different distances from the wall where the force data will be collected. Therefore, once the CFD model has been validated, it can be extended to analyse a larger number of tilt angles.

4.2. Flow field visualization

In order to model the aerodynamic ground effect of tilted rotors, it is necessary to consider a large range of θ. The CFD model, validated in the previous section, has been used to simulate new rotor inclinations. Additionally, numerical simulations help to visualise the flow field and provide information on the behaviour of the fluid. Changes in the flow field of a propeller lead to changes in performance. This analysis has been performed up to an angle of 40°, since above this value the ground effect is negligible and the thrust ratio is close to 1 for all distances z. For angles of 20° and 30° the minimum distance simulated is $0.75R$ and for 35° and 40° it is $1R$ since for smaller values the rotational domain intersects with the stationary domain.

Fig. 13 shows the thrust ratio of a rotor under IGE and OGE conditions for a wide range of inclinations [0° − 40°] and distances to the ground plane (z/R = 0.6, 0.75, 1, 1.5, 1.5, 2, 2.5, 3, 3.5, 4 and 5). These results are compared with others ground effect models developed in the past [18,24,45]. It can be seen, the thrust ratio T_{IGE}/T_{OGE} decreases with increasing tilt angle. The increased thrust becomes more noticeable as the rotor approaches the ground. To understand the physical phenomena that cause this change of thrust with the inclination, Fig. 14 presents the velocity magnitude (m/s) contours and vectors for the non-dimensional height $z/R = 1$. The vectors show the direction of the flow. Furthermore, streamlines are depicted to illustrate the wake structures in detail. The downwash pattern for both the co-planar and tilted single rotor configurations ($\theta = 0°$ and θ = 10°, 20°, 30°, 40° respectively) are plotted in Fig. 14. On the one hand, a smaller number of streamlines is displayed in the central area where the direction of the vortex structures can be distinguished. On the other hand, on the right-hand side, a large number of streamlines are drawn where all formed vortices are clearly visible.

As the rotor is close to the ground, the rotor wake is restricted in the axial direction and cannot expand downwash freely as it would in a free environment. The ground causes the flow to expand radially when it reaches it due to the no-slip condition. The interaction between flow and ground plane resulted in the formation of vortex structures underneath the rotor so-called ground vortex [49]. The thrust increase of a rotor is mainly related to the reduction of the downwash under the propeller near the ground. Fig. 14 shows that when the rotor is positioned parallel to the ground ($\theta = 0°$), two downstream vortices appear in the wake with a larger size than in the other cases ($\theta \neq 0°$). For values $\theta > 0°$, an asymmetric flow pattern concerning the rotation axis is produced. At the same time, the recirculation of two flow sub-structures is found in the centre of the propeller, as observed with the numerical method proposed in [45]. In contrast to the co-planar case, the angle of inclination (θ) causes the wake of the rotor to behave differently on the downward and upward side of the propeller.

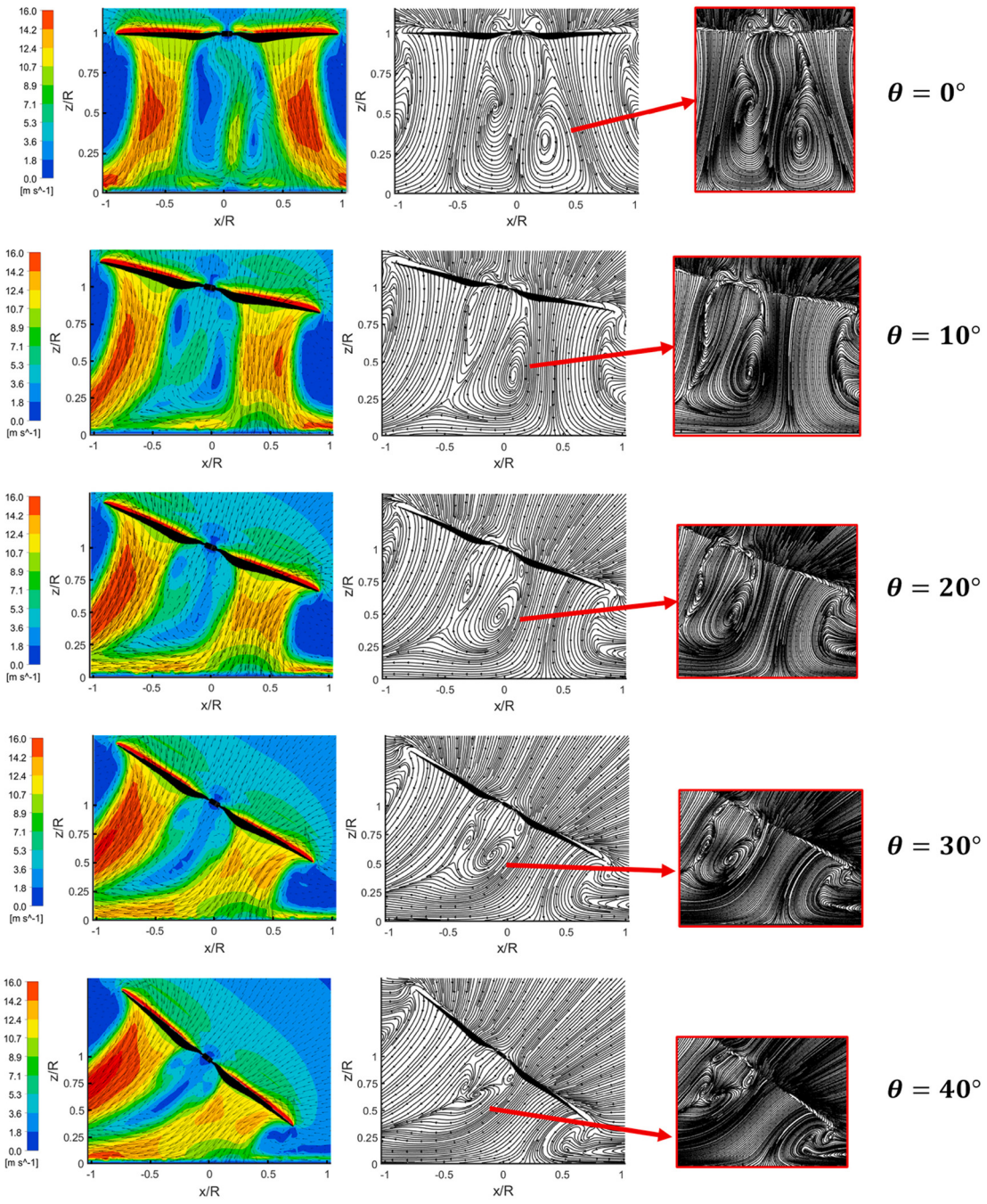

Fig. 14. Visualisation of the velocity contours and vectors on the left-hand side. Streamlines in the middle and right-hand figures. All the results correspond to different rotor inclinations ($\theta = 0°$, 10°, 20°, 30°, 40°) for the distance $1R$ measured from the centre of rotation of the propeller to the ground.

On the one hand, on the downward side (propeller tip is closer to the ground), the tip-vortex intersects with the ground causing vortex contraction. On the other hand, on the upward side (propeller tip farther from the ground), the wake expands outward freely, becoming increasingly asymmetric as the inclination increases. Hence, the flow is accelerated on the upstream side, causing the velocities to be higher, as shown in the velocity contour in Fig. 14. This expansion causes the size of the two dominant vortices to decrease with increasing tilt. Moreover, the downwash under the propeller is less constrained as inclination increases. It will lead to a progressive decrease of ground effect with θ (see Fig. 13).

Additionally, Fig. 15 shows the velocity contour in four sections parallel to the ground. It can be seen how the velocity distribution changes for each angle (θ) and height (z). The velocity flow field of the co-planar case is compared with the inclined case. The progressive increase in velocities on the upward side is highlighted, as shown in Fig. 14. In addition, an asymmetry in the flow field is also apparent. As expected, the flow is spread radially near the ground ($3R/20$), reducing the size of the vortices. To support Fig. 15, the vorticity contour near the ground has been drawn in Fig. 16. It allows to quantify the turbulent flow. When $\theta = 0$, the two dominant vortices displayed in the streamline flow field in Fig. 14 are visible. These vortices diminish as they approach the ground. Conversely, as θ increases, the tip vortex, which is located closer to the ground, becomes more noticeable. For a certain height, the higher θ, the nearer the propeller is to the surface. Also, as the height z rises, these vortices become smaller as a result of their spreading.

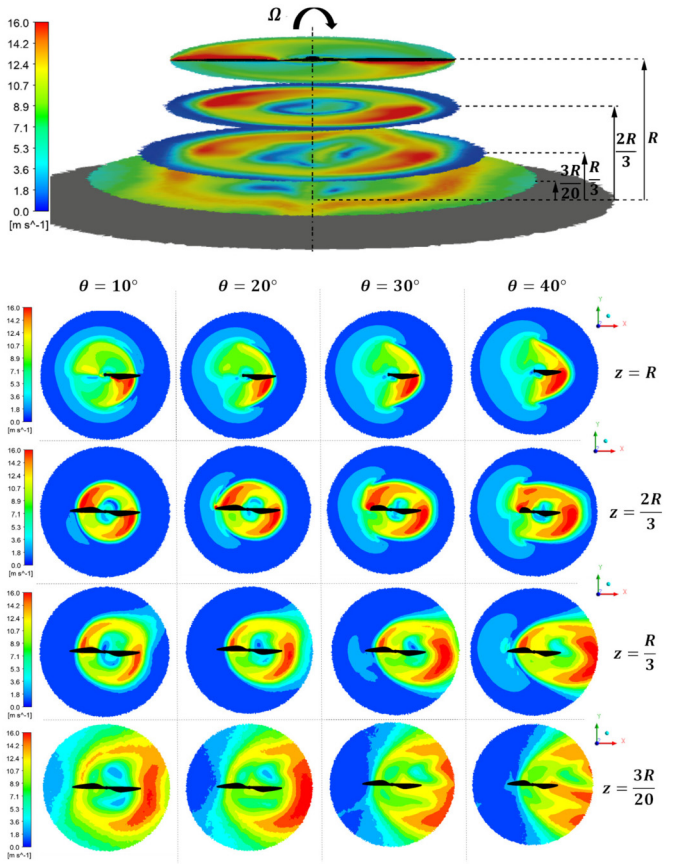

Fig. 15. Velocity contour for several angles of inclination (θ) at different sections parallel to the ground.

Regarding vortex dissipation, higher-order schemes allow more detail on the formation of vortex structures in the vicinity of the ground due to their dissipative nature. However, Fig. 17 shows that the strength of the blade tip vortices is dissipated mainly in the stationary domain when θ = 0. This could be due to the use of the gradient-diffusion approximation of the turbulence schemes [71]. These results are in agreement with those presented by [49] for higher-order schemes. On the contrary, for values $\theta > 0$, the blade tip vortex dissipation becomes asymmetric. Increasing the angle causes the vortex dissipation to be anticipated.

Next, the wake inflow distribution at the rotor disc will be examined for each rotor tilt. The inflow distribution is affected by the operating conditions. In particular, it plays an important role when operating close to surfaces, as the rotor load is influenced and, as a consequence, the effective angle of attack of each blade cross-section. Fig. 18 shows the radial distribution of axial induced velocities normalised to the hover induced velocity (V_h) for the non-dimensional height $z/R = 1$. The hover induced velocity is defined as $V_h = \Omega R\sqrt{C_T/2}$.

Mainly, the induced velocities changes near the blade tip. First, it is observed that when $\theta = 0$, the radial distribution is symmetrical on both sides of the propeller. Then, it is noted that the axial induced velocity increases on the upward side as the rotor tilt increases. An opposite trend occurs on the downward side, where induced velocities decrease smoothly as θ increases. These results are in good agreement with those presented by [42,45]. However, in the current study, the increase in inflow on the upward side is greater than the decrease in inflow on the downward side, a contrary behaviour was observed by Xin [42]. Indeed, a reduction of the axial induced velocity results in an increase of the local thrust and the other way around [20,44]. Consequently, the inflow distribution is in agreement with the thrust results in Fig. 13, since there is a progressive increase of the induced velocities with angle (θ) which is much more noticeable than the decrease. This behaviour leads us to assume that the thrust ratio will progressively decrease with (θ).

This analysis reveals that MRF is able to predict the formation of two dominant vortices near the ground. For $\theta > 0°$, the MRF method shows the change in the size and shape of the vortices, revealing the asymmetric behaviour of the flow as in previous work [45]. Furthermore, the change in inflow distribution with θ is properly predicted. Nevertheless, the MRF method is a stationary approximation and is not able to consider the non-stationary flow and the transient phenomena that may appear.

5. Modelling

5.1. Model identification

Cheeseman and Bennett's expression (see Eq. (4)) has been modified to capture the effect of the angle of inclination of tilted propellers under the aerodynamic ground effect. In [18] the rotor is represented as a point source and the method of images is applied to simulate the ground. The image rotor will cause the induced velocity of the original rotor to be modified:

$$v_{IGE} = v_{i\infty} - \delta v_i(z) \tag{5}$$

where v_{IGE} is the induced velocity in ground effect (IGE) and $v_{i\infty}$ is the induced velocity when the influence of the ground is negligible. $\delta v_i(z)$ is the induced velocity on the rotor at a distance z from the ground caused by the image rotor, and is defined as $\delta v_i(z) = A v_{i\infty}/16\pi z^2$, being A the area of the rotor disk. In this work, a model is proposed where the following assumptions are made:

Assumption 1: After demonstrating that the Cheeseman and Bennett theory is in good agreement with experimental and simulation results for low Reynolds number propellers, a modification of this theory is proposed that takes into account the rotor tilt angle. For this purpose, it is considered that the strength of the source (δv_i) must be a function that depends on both the distance z and the rotor tilt angle (θ):

$$\delta v_i(z,\theta) = \frac{A v_{i\infty} \cdot f_c(\theta)}{16\pi z^2} \tag{6}$$

where $f_c(\theta)$ is the function to be determined in this section. Thus, the thrust ratio becomes:

$$\left[\frac{T_{IGE}}{T_{OGE}}\right]_{(z,\theta)} = \frac{1}{1 - \dfrac{\delta v_i(z,\theta)}{v_{i\infty}}} = \frac{1}{1 - \left(\dfrac{R}{4z}\right)^2 \cdot f_c(\theta)} \tag{7}$$

Assumption 2: from Fig. 13, it is known that the function $f_c(\theta)$ must be:

$$\begin{aligned} &f_c(\theta) \approx 1 \quad \text{if} \quad \theta = 0, 2\pi, 4\pi, .., n\pi \\ &f_c(\theta) < 1 \quad \text{if} \quad 0 < \theta \leq \frac{2}{9}\pi \end{aligned} \tag{8}$$

It is assumed that the Eq. (7) should be close to the theory predicted by Cheeseman and Bennett (see Eq. (4)) when $\theta = 0°$. Under these conditions, the function f_c will not be exactly 1 since for values close to the ground (z = 0.6R) the experimental and simulation results deviate from Cheeseman's theory. This discrepancy has been observed in other analyses presented in the past [30]. The proposed model will allow a correction to be made to the classical theory for small-scale propellers at low Reynolds numbers typically used in UAVs.

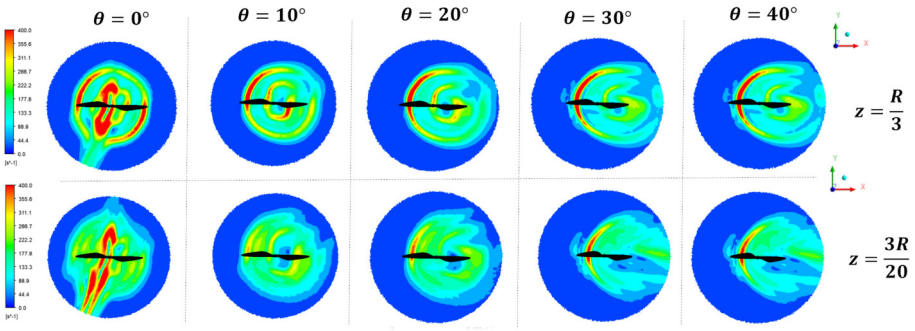

Fig. 16. Vorticity contour for various tilt angles in two sections close to the ground.

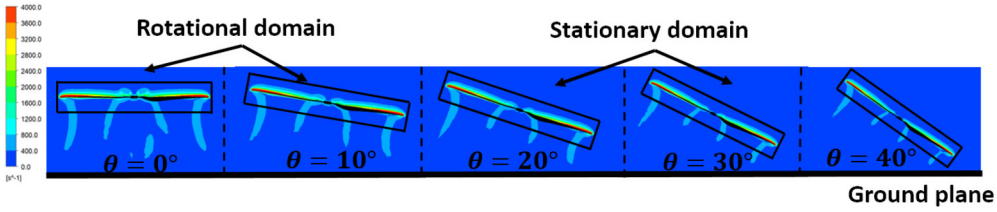

Fig. 17. Vorticity contour for various tilt angles in a plane perpendicular to the rotor disc. Findings for dimensionless height $z/R = 1$.

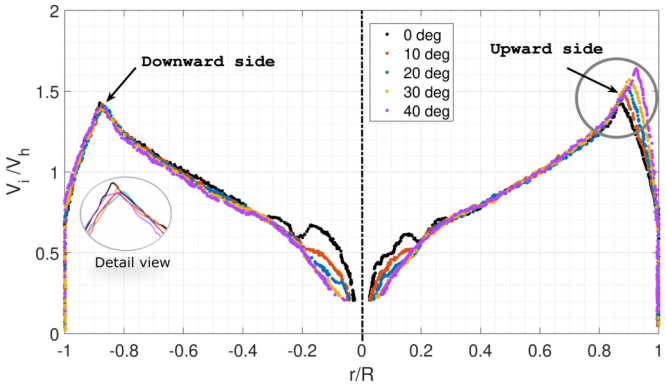

Fig. 18. Wake inflow distribution on the rotor disk at various inclinations of the rotor and for non-dimensional height $z/R = 1$.

In previous work, Chen [72] showed different inflow models for forward, hovering, vertical and low-speed flight. The first harmonic inflow models were found to fit well with experimental results obtained in wind tunnels. Subsequently, other authors investigated the applicability of induced velocity models both for analysing helicopter autorotation [73] and in small-scale propellers with oblique flow [74]. Following this line, and according the boundary conditions defined in Eq. (8), the function $f_c(\theta)$ is defined as a linear combination of trigonometric functions:

$$f_c(\theta) = a_0 + \sum_{m=1}^{\infty} a_m \cdot sin(m\theta) + \sum_{m=1}^{\infty} b_m \cdot cos(m\theta) \tag{9}$$

where, a_0, b_m and a_m are real components and independent of θ. As in previous work [72], it is found that the first harmonic is sufficiently accurate and provides a good fit to the simulation results. Therefore, $m = 1$ in the function $f_c(\theta)$. The downwash of the rotor due to its image will change for each angle and can be expressed as:

$$\delta v_i(z,\theta) = \frac{A v_{i\infty} \cdot (a_0 + a_1 \cdot sin\theta + b_1 \cdot cos\theta)}{16\pi z^2} \tag{10}$$

The gradient descent algorithm with multiple variables is used to obtain the coefficients a_0, a_1, b_1 and can be expressed as follows:

$$\beta_j := \beta_j - \gamma \frac{\partial}{\partial \beta_j} J(\beta_0, \beta_1, \beta_2,), \quad j = 0, 1, 2 \tag{11}$$

where γ is the learning rate, β_0, β_1 and β_2 are a_0, a_1 and b_1 respectively, and $J(\beta_0, ..., \beta_j)$ is the differentiable and multi-variable cost function:

$$J(\beta_j) = \frac{1}{2s} \sum_{i=1}^{s} (h_\beta(z^i, \theta^i) - y^i)^2 \tag{12}$$

where $y^i = T_{IGE}/T_{OGE}$ is obtained from the CFD numerical analysis, s is the number of samples and $h_\beta(z^i, \theta^i)$ is the hypothesis function that contains the coefficients to be determined (a_0, a_1, b_1) and will depend on the height z and the angle of inclination θ:

$$h_\beta(z^i, \theta^i) = \frac{1}{1 - \left(\frac{R}{4z}\right)^2 \cdot (a_0 + a_1 \cdot sin\theta + b_1 \cdot cos\theta)} \tag{13}$$

To implement the algorithm, it is necessary to perform the partial derivatives of Eq. (12) for each of the variables of interest (β_j). The coefficients resulting from the application of the gradient descent algorithm are as follows:

$$\begin{aligned} a_0 &= 0.415 \\ a_1 &= -0.712 \\ b_1 &= 0.361 \end{aligned} \tag{14}$$

Fig. 19 depicts the thrust ratio curves (T_{IGE}/T_{OGE}) obtained with the proposed ground effect model for angles θ = 0°, 5°, 10°, 15°, 20°, 25°, 30°, 35° and 40° and for non-dimensional distances z/R = 0.6, 0.75, 1, 1.5, 1.5, 2, 2.5, 3, 3.5, 4, 5 and are compared with CFD simulations. Furthermore, the proposed model is checked against experimental results for angles 0°, 10°, 20°, 30°. It can be seen that data-driven model is in good agreement with both numerical simulations and experimental results. In all cases, the errors produced are less than 3%, with the largest errors occurring at the distances closest to the ground.

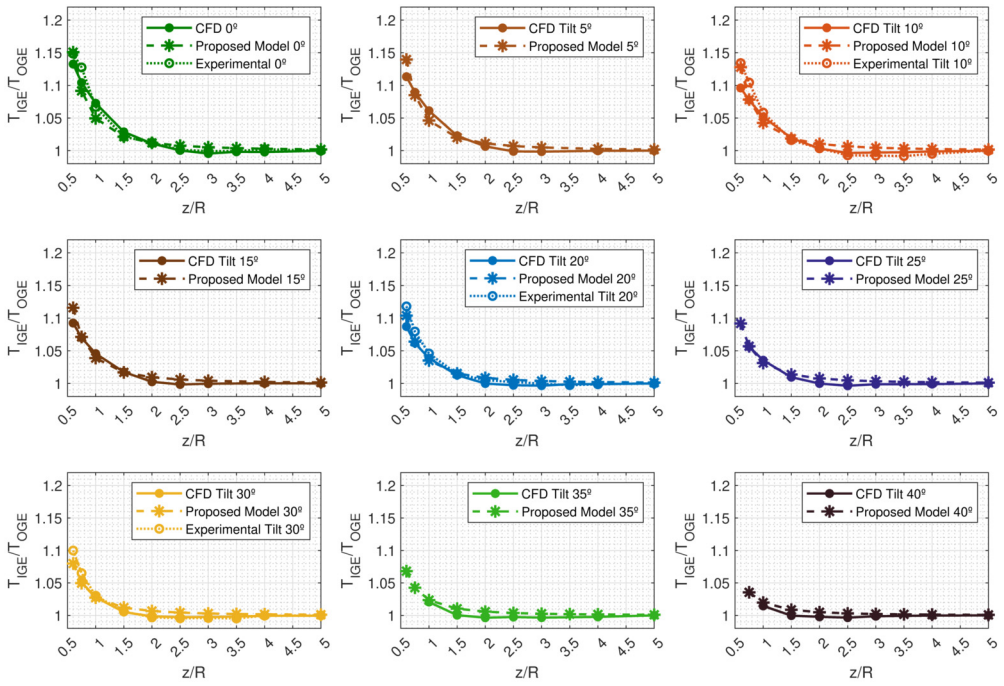

Fig. 19. Comparison of the simulated thrust ratio T_{IGE}/T_{OGE} and that achieved with the proposed model in Eq. (7) and the parameters (14) for the eight angles investigated in CFD (θ = 0°, 5°, 10°, 15°, 20°, 25°, 30°, 35° and 40°) and ten distances from the ground.

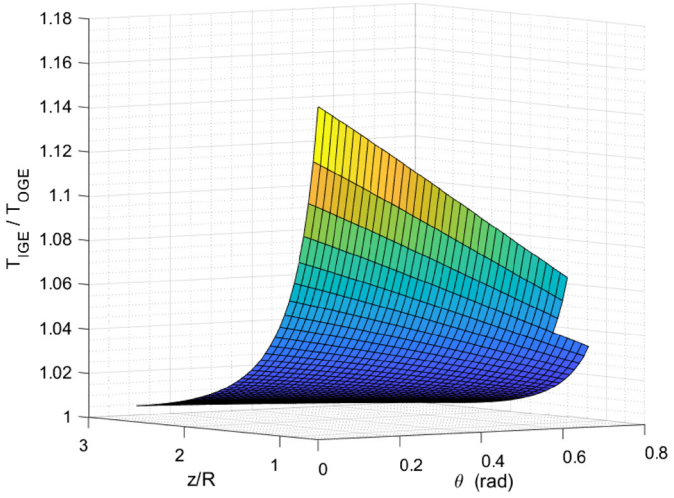

Fig. 20. 3D map representation of the results obtained after applying the proposed model (Eq. (7) and the parameters (14)) for a sweep of tilt angles and dimensionless distances. The Z axis corresponds to the T_{IGE}/T_{OGE} ratio and the X and Y axes show the dimensionless distance (z/R) and the tilt angle (θ) respectively.

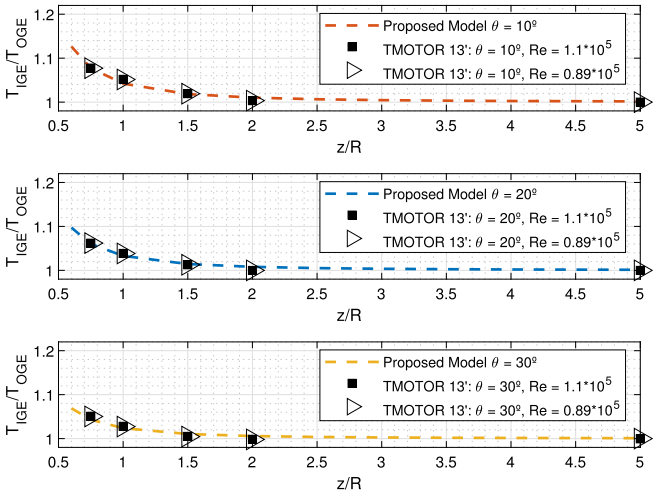

Fig. 21. Thrust ratio T_{IGE}/T_{OGE} achieved for the proposed model in Eq. (7) and the parameters (Eq. (14)). These results are compared with those obtained for the T-Motor propeller 13X4.4 for angles θ = 10°, 20°, 30°, non-dimensional distances from the ground $z/R = 0.75, 1, 1.5, 2, 5$ and two different Reynold numbers.

Fig. 20 plots the predicted thrust ratio by the proposed model for a sweep of angles between 0° and 40° and for z/R distances between 0.6 and 3, except for angles from 35° to 40° whose distances vary from 0.75 to 3. This leap can be seen in the 3D representation in Fig. 20.

5.2. Verification of the proposed ground effect model

In order to validate the proposed model for low Reynolds numbers propellers with different geometries and dimensions, 45 numerical simulations were carried out. In this study, two new propellers have been evaluated: T-Motor 18x6.1 and APC 9x4.4, whose characteristics were presented in section 2.1. For this analysis, the angles 10°, 20°, 30° and the non-dimensional heights 0.75, 1, 1.5, 2 and 5 have been considered. Additionally, the proposed model has been verified for different Reynolds numbers.

Fig. 21 presents the T_{IGE}/T_{OGE} ratio for different Reynolds number in T-Motor 13x4.4. Also, in Fig. 22 the thrust ratios for various Re in APC 9x4.4 and T-Motor 18x6.1 propellers are given. These results are compared with those obtained from the model defined in Eq. (7) and the parameters given in the expression (14). It can be noted that the model presented in the previous section fits with good accuracy to propellers with other geometries and sizes. Furthermore, the influence of the Reynold number for each propeller is negligible. The errors found for all cases are less than 1%.

The model can be used when $\theta = 0°$, applying a correction to classical theory, and up to a maximum angle of 40°. The ground distance at which the proposed model can be operated is from

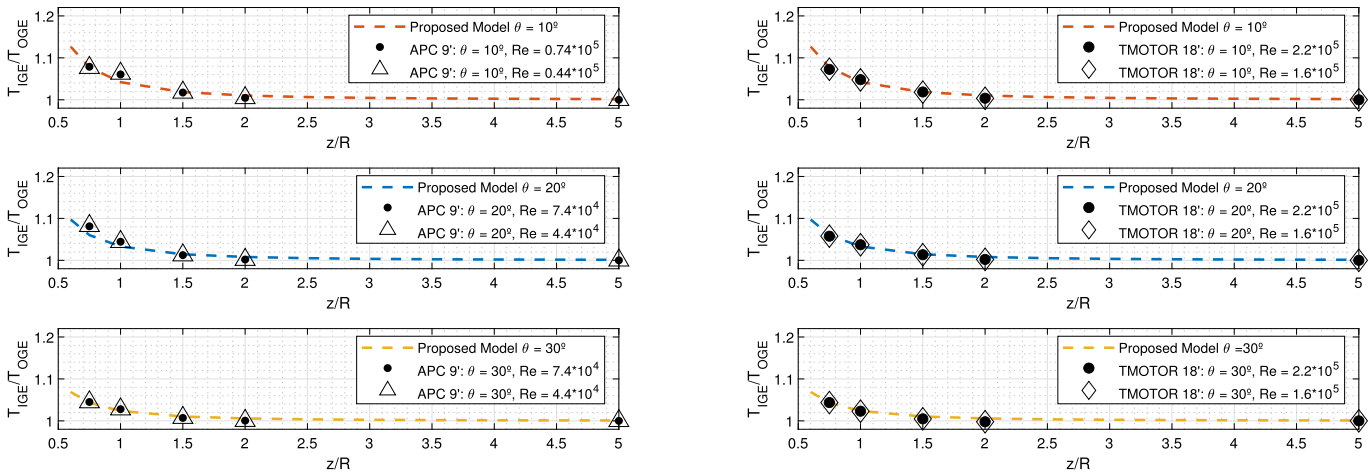

Fig. 22. Thrust ratio T_{IGE}/T_{OGE} achieved for the proposed model in Eq. (7) and the parameters (Eq. (14)). These results are compared with those obtained for the APC 9x4.4 and T-Motor 18x6.1 propellers for angles θ = 10°, 20°, 30°, non-dimensional distances from the ground $z/R = 0.75, 1, 1.5, 2, 5$ and two different Reynold numbers.

$0.6R$ to $5R$ for $0° \leq \theta \leq 35°$, from $0.75R$ to $5R$ for $35° < \theta \leq 40°$. There are two limits to the application of the model since for angles greater than 35°, $z/R \geq 0.75$ so that the propeller does not collide with the ground. Above the distance $5R$, the thrust ratio (T_{IGE}/T_{OGE}) remains constant.

6. Discussion and limitations

The ground effect model with inclined rotors developed in the previous section allows to compensate for the thrust increase experienced by a rotor when operating close to the ground. The main interest of this model lies in its future implementation in a model-based control or else, be used for optimal trajectory planning. This could improve the behaviour of UAV controllers in confined environments.

The proposed model is the first ground effect analysis of tilted small-scale propellers. It gives a good understanding of how the flow behaves and how this causes changes the thrust experienced by the rotors. First, this model would be the starting point for future models of fully actuated multirotor configurations with tilted propellers. This process has been carried out by other authors [20], where they have previously analysed the parameters of interest in a single-rotor to take as a starting point for a multirotor. It is necessary to know the influence of the variables understudy in the simplest case in order to be able to extrapolate the model to more complex scenarios.

Secondly, the proposed model could be applied when a complete multirotor is under the so-called partial ground effect as it was done by Sanchez et al. in [28]. In this situation, only one UAV rotors are above the ground plane generating a disturbance torque due to the aerodynamic ground effect that could compromise the performance of the controller. In Sanchez et al. [28] included the classical Cheeseman and Bennet model in the controller to improve the robot controllability. The proposed model could be used to compensate for the partial ground effect of a multirotor with tilted propellers in the same way.

According to previous sections and as Pasquali pointed out in [45], considering rotor tilt on planar surfaces is equivalent to using co-planar rotors on inclined surfaces. Under this assumption, on the one hand, when a multirotor with co-planar rotors operate on inclined surfaces, it happens that one or several of its rotors are very close to the surface while the rest could be at a distance greater than 2R, where the influence of the ground is negligible. In these cases, the presented ground effect model would be useful to be taken into account in the controller. While there are rotors that do not suffer from ground influence, there could be one or more that are affected by ground tilting. In this case, partial ground effect could also appear and the model would still be useful. On the other hand, an aerial platform with planar rotors may tilt concerning a horizontal surface and be subject to the same effects as those discussed above. In all these cases, the ground effect model derived from CFD simulations would be applicable.

In conclusion, although the presented model has been validated for propellers between 9 and 18 inches with Reynolds numbers in the range $[0.46 - 2.2] \cdot 10^5$, it is possible to find a wide variety of situations in which the proposed model and this research work could be useful.

7. Conclusions and future work

Experimental tests and numerical simulations have made it possible to analyse the aerodynamic performance of small-scale rotors tilted at low Reynolds numbers close to the ground. The flow behaviour in this scenario is different from the classical rotor parallel to the ground. There is a lack of information on how the forces of a tilted rotor change as it approaches the ground. Therefore, a wide range of rotor inclinations (θ) and ground distances (z/R) were tested. Experimentation allows for validation of simulation results and to define of a CFD scenario to examine the ground effect with little effort. Finally, we propose a ground effect model for tilted rotors by modifying the Cheeseman and Bennett theory.

The CFD results are in good agreement with the experimental results extracted from the test stand set up for this study. It is proven that a steady-state approximation is sufficient to capture the forces of a rotor in the vicinity of the ground when there are no external disturbances. The computational costs associated with the multi-zone MRF method are small compared to the structural assembly and testing on a test stand.

The results gathered throughout this research show that the thrust force of a small-scale propeller increases as it approaches the ground at any angle. This trend is also aligned with the presented vortices structure analysis. However, as the tilt angle increases, the thrust forces in the vertical direction decrease while the horizontal component becomes more and more noticeable. Furthermore, the Cheeseman and Bennett theory is also compared with the CFD results showing satisfactory outcomes when the rotor is placed parallel to the ground. Nevertheless, in the case of inclination rotors, the classical theory does not provide an accurate estimation of the ground effect. It is demonstrated that the thrust

ratio decreases with respect to the classical theory as the angle increases. The developed model fits the results obtained from the numerical simulations with good accuracy.

In future works, the proposed model for tilted rotors will be implemented in control laws in order to compensate for this effect when UAVs operate close to the ground. This will result in safer flights by avoiding instabilities in the aerial platform.

Declaration of competing interest

The authors declare the following financial interests/personal relationships which may be considered as potential competing interests:

Ambar Garofano-Soldado reports financial support was provided by University of Seville. Ambar Garofano-Soldado reports a relationship with University of Seville that includes: employment.

Acknowledgements

This work has been supported by the H2020 RESIST (H2020-MG-2017-769066) and PILOTING (H2020-ICT-2019-2-871542) projects, funded by the European Commission and the ARTIC Project (RTI2018-102224-B-I00), funded by the Spanish Agencia Estatal de Investigación. The work of Ambar Garofano-Soldado is supported by the FPI grant (PRE2019-089812) from the Ministry of Science and Innovation of the Spanish Government.

References

[1] K.P. Valavanis, G.J. Vachtsevanos, Handbook of Unmanned Aerial Vehicles, vol. 2077, Springer, 2015.
[2] E. Semsch, M. Jakob, D. Pavlicek, M. Pechoucek, Autonomous UAV surveillance in complex urban environments, in: 2009 IEEE/WIC/ACM International Joint Conference on Web Intelligence and Intelligent Agent Technology, vol. 2, IEEE, 2009, pp. 82–85.
[3] N.H. Motlagh, M. Bagaa, T. Taleb, Uav-based IoT platform: a crowd surveillance use case, IEEE Commun. Mag. 55 (2) (2017) 128–134.
[4] J. Seo, L. Duque, J. Wacker, Drone-enabled bridge inspection methodology and application, Autom. Constr. 94 (2018) 112–126.
[5] Y. Li, C. Liu, Applications of multirotor drone technologies in construction management, Int. J. Constr. Manag. 19 (5) (2019) 401–412.
[6] I. Mademlis, N. Nikolaidis, A. Tefas, I. Pitas, T. Wagner, A. Messina, Autonomous unmanned aerial vehicles filming in dynamic unstructured outdoor environments [applications corner], IEEE Signal Process. Mag. 36 (1) (2018) 147–153.
[7] V. Krátký, A. Alcántara, J. Capitán, P. Štěpán, M. Saska, A. Ollero, Autonomous aerial filming with distributed lighting by a team of unmanned aerial vehicles, IEEE Robot. Autom. Lett. 6 (4) (2021) 7580–7587.
[8] W.-C. Chiang, Y. Li, J. Shang, T.L. Urban, Impact of drone delivery on sustainability and cost: realizing the UAV potential through vehicle routing optimization, Appl. Energy 242 (2019) 1164–1175.
[9] A.E. Jimenez-Cano, P.J. Sanchez-Cuevas, P. Grau, A. Ollero, G. Heredia, Contact-based bridge inspection multirotors: design, modelling, and control considering the ceiling effect, IEEE Robot. Autom. Lett. 4 (4) (2019) 3561–3568, https://doi.org/10.1109/LRA.2019.2928206.
[10] M.Á. Trujillo, J.R. Martínez-de Dios, C. Martín, A. Viguria, A. Ollero, Novel aerial manipulator for accurate and robust industrial ndt contact inspection: a new tool for the oil and gas inspection industry, Sensors 19 (6) (2019) 1305.
[11] L. Wawrla, O. Maghazei, T. Netland, Applications of drones in warehouse operations, Whitepaper, ETH Zurich, D-MTEC, 2019.
[12] A. Ollero, M. Tognon, A. Suarez, D. Lee, A. Franchi, Past, present, and future of aerial robotic manipulators, IEEE Trans. Robot. (2021).
[13] P. Sanchez-Cuevas, G. Heredia, A. Ollero, Multirotor aerodynamic effects in aerial manipulation, in: Aerial Robotic Manipulation, Springer, 2019, pp. 67–82.
[14] A. Betz, The ground effect on lifting propellers, National Advisory Committee for Aeronautics, Washington, DC, USA Technical report 835, 1972.
[15] A. Matus-Vargas, G. Gamez, J. Martinez-Carranza, Ground effect on rotorcraft unmanned aerial vehicles: a review, Intell. Serv. Robot. 14 (2021) 1–20, https://doi.org/10.1007/s11370-020-00344-5.
[16] H. Knight, R.A. Hefner, Analysis of ground effect on the lifting airscrew, Tech. Rep. 835, NACA TN, 1941.
[17] J. Zbrozek, Ground effect on the lifting rotor, Technical report 2347, British ARC and RM, 1947.
[18] I. Cheeseman, W. Bennett, The effect of ground on a helicopter rotor in forward flight, ARC R&M 3021, 1955.
[19] H.H. Heyson, Ground effect for lifting rotors in forward flight, Technical report NASA-TN-D-234, National Aeronautics and Space Administration, Hampton, VA, USA, May 1960.
[20] X. He, G. Kou, M. Calaf, K. Leang, In-ground-effect modelling and nonlinear disturbance observer for multi-rotor UAV control, J. Dyn. Syst. Meas. Control 141 (2019), https://doi.org/10.1115/1.4043221.
[21] J.S. Hayden, The effect of the ground on helicopter hovering power required, in: American Helicopter Society 32th Annual National V/STOL Forum Proceedings, Montreal, Canada, May 1976.
[22] H.M. Curtiss, W.F. Putman, E. Hanker, Rotor aerodynamics in ground effect at low advance ratios, J. Am. Helicopter Soc. 29 (1) (1984) 48–55, https://doi.org/10.1109/TRO.2018.2821155.
[23] A. Graber, A. Rosen, A. Seginer, An investigation of a hovering rotor in ground effect, Aeronaut. J. 95 (945) (1991) 161–169, https://doi.org/10.1017/S0001924000023812.
[24] J.S. Light, Tip vortex geometry of a hovering helicopter rotor in ground effect, J. Am. Helicopter Soc. 38 (1989) 34–42.
[25] D. Griffiths, S. Ananthan, J. Leishman, Predictions of rotor performance in ground effect using a free-vortex wake model, J. Am. Helicopter Soc. 50 (2005) 302–314, https://doi.org/10.4050/1.3092867.
[26] N. Itoga, N. Iboshi, M. Horimoto, S. Saito, Y. Tanabe, Numerical analysis of helicopter rotor hovering in close proximity to the ground with a wall, J. Jpn. Soc. Aeronaut. Space Sci. 58 (2010) 269–276, https://doi.org/10.2322/jjsass.58.269.
[27] T. Lee, J. Leishman, M. Ramasamy, Fluid dynamics of interacting blade tip vortices with a ground plane, J. Am. Helicopter Soc. 55 (2010) 022005, https://doi.org/10.4050/JAHS.55.022005.
[28] P. Sanchez-Cuevas, G. Heredia, A. Ollero, Characterization of the aerodynamic ground effect and its influence in multirotor control, Int. J. Aerosp. Eng. (2017), https://doi.org/10.1155/2017/1823056.
[29] I. Sharf, M. Nahon, A. Harmat, W. Khan, M. Michini, N. Speal, M. Trentini, T. Tsadok, T. Wang, Ground effect experiments and model validation with draganflyer x8 rotorcraft, in: 2014 International Conference on Unmanned Aircraft Systems (ICUAS), 2014, pp. 1158–1166.
[30] S.A. Conyers, M.J. Rutherford, K.P. Valavanis, An empirical evaluation of ground effect for small-scale rotorcraft, in: 2018 IEEE International Conference on Robotics and Automation (ICRA), 2018, pp. 1244–1250.
[31] C. Powers, D. Mellinger, A. Kushleyev, B. Kothmann, V. Kumar, Influence of Aerodynamics and Proximity Effects in Quadrotor Flight, Springer International Publishing, 2013, pp. 289–302.
[32] X. He, K. Leang, Quasi-steady in-ground-effect model for single and multirotor aerial vehicles, AIAA J. 58 (2020), https://doi.org/10.2514/1.J059223.
[33] J. Cai, S. Gunasekaran, M. Ol, A. Ahmed, Propellers in partial ground effect, in: APS Division of Fluid Dynamics Meeting Abstracts, APS Meeting Abstracts, 2019, B09.005.
[34] A. Garofano-Soldado, G. Heredia, A. Ollero, Aerodynamic interference in confined environments with tilted propellers: wall effect and corner effect, in: 2021 Aerial Robotic Systems Physically Interacting with the Environment (AIRPHARO), 2021, pp. 1–8.
[35] C. Hooi, F. Lagor, D. Paley, Flow sensing for height estimation and control of a rotor in ground effect: modelling and experimental results, in: Annual Forum Proceedings - AHS International, vol. 3, 2015, pp. 1878–1889.
[36] H. Keshavarzian, K. Daneshjoua, Modified under-actuated quadrotor model for forwarding flight in the presence of ground effect, Aerosp. Sci. Technol. 89 (2019), https://doi.org/10.1016/j.ast.2019.04.001.
[37] M. Ryll, D. Bicego, M. Giurato, M. Lovera, A. Franchi, Fast-hex – a morphing hexarotor: design, mechanical implementation, control and experimental validation, IEEE/ASME Trans. Mechatron. (2021) 1, https://doi.org/10.1109/TMECH.2021.3099197.
[38] G. Michieletto, M. Ryll, A. Franchi, Fundamental actuation properties of multirotors: force–moment decoupling and fail–safe robustness, IEEE Trans. Robot. 34 (3) (2018) 702–715, https://doi.org/10.1109/TRO.2018.2821155.
[39] S. Rajappa, M. Ryll, H.H. Bülthoff, A. Franchi, Modeling, control and design optimization for a fully-actuated hexarotor aerial vehicle with tilted propellers, in: 2015 IEEE International Conference on Robotics and Automation (ICRA), 2015, pp. 4006–4013.
[40] M. Ryll, G. Muscio, F. Pierri, E. Cataldi, G. Antonelli, F. Caccavale, D. Bicego, A. Franchi, 6d interaction control with aerial robots: the flying end-effector paradigm, Int. J. Robot. Res. 38 (9) (2019) 1045–1062.
[41] E. Fradenburgh, The helicopter and the ground effect machine, J. Am. Helicopter Soc. 5 (4) (1960) 26–28.
[42] H. Xin, J. Prasad, D. Peters, N. Itoga, N. Iboshi, T. Nagashima, Ground effect aerodynamics of lifting rotors hovering above inclined ground plane, in: 17th Applied Aerodynamics Conference, 1999.
[43] S. Platzer, J. Rauleder, Investigation on hovering rotors over inclined ground planes - a computational and experimental study, in: 44th Eur. Rotorcr. Forum 2018, ERF 2018, vol. 1, September 2018.
[44] J.I. Milluzzo, A. Martinez, S. Drayton, S. Davids, Experimental investigation of rotors hovering above inclined surfaces, J. Am. Helicopter Soc. 66 (2) (2021), https://doi.org/10.4050/jahs.66.022005.
[45] C. Pasquali, J. Serafini, G. Bernardini, J. Milluzzo, M. Gennaretti, Numerical-experimental correlation of hovering rotor aerodynamics in ground effect,

Aerosp. Sci. Technol. 106 (2020) 106079, https://doi.org/10.1016/j.ast.2020.106079.
[46] V. Lakshminarayan, T. Kalra, J. Baeder, Detailed computational investigation of a hovering microscale rotor in ground effect, AIAA J. 51 (2013) 893–909, https://doi.org/10.2514/1.J051789.
[47] S. Nair, C. Joseph, R. Mohan, An evaluation of ground effect modelling for rotors in hover, in: 6th Asian/Australian Rotorcraft Forum/Heli Japan 2017, Kanazawa, Japan, November 2017.
[48] C. Paz, E. Suarez, C. Gil, C. Baker, Cfd analysis of the aerodynamic effects on the stability of the flight of a quadcopter UAV in the proximity of walls and ground, J. Wind Eng. Ind. Aerodyn. 206 (2020) 104378, https://doi.org/10.1016/j.jweia.2020.104378.
[49] P.A. Silva, P. Tsoutsanis, A.F. Antoniadis, Simple multiple reference frame for high-order solution of hovering rotors with and without ground effect, Aerosp. Sci. Technol. 111 (2021) 106518, https://doi.org/10.1016/j.ast.2021.106518.
[50] M. Costes, T. Renaud, B. Rodriguez, Rotorcraft simulations: a challenge for CFD, Int. J. Comput. Fluid Dyn. 26 (6–8) (2012) 383–405, https://doi.org/10.1080/10618562.2012.726710.
[51] Z. Liu, R. Albertani, J.-M. Moschetta, C. Thipyopas, M. Xu, Experimental and computational evaluation of small microcoaxial rotor in hover, J. Aircr. 48 (2011) 220–229, https://doi.org/10.2514/1.C031068.
[52] E. Loureiro, N. Oliveira, P. Hallak, F. Bastos, L. Rocha, R. Delmonte, A. Lemonge, Evaluation of low fidelity and CFD methods for the aerodynamic performance of a small propeller, Aerosp. Sci. Technol. 108 (2021) 106402, https://doi.org/10.1016/j.ast.2020.106402.
[53] H.A. Kutty, P. Rajendran, 3D CFD simulation and experimental validation of small APC slow flyer propeller blade, Aerospace 4 (1) (2017), https://doi.org/10.3390/aerospace4010010.
[54] M. Stajuda, M. Karczewski, D. Obidowski, K. Jóźwik, Development of a CFD model for propeller simulation, Mech. Mech. Eng. 20 (2016).
[55] M. Rostami, A. hamzeh Farajollahi, Aerodynamic performance of mutual interaction tandem propellers with ducted UAV, Aerosp. Sci. Technol. 108 (2021) 106399, https://doi.org/10.1016/j.ast.2020.106399, https://www.sciencedirect.com/science/article/pii/S1270963820310816.
[56] X. Wang, Y. Liu, C. Huang, Research on finite ground effect of a rotor, in: 2019 IEEE/RSJ International Conference on Intelligent Robots and Systems (IROS), 2019, pp. 6935–6940.
[57] H. Yao, H. Zhang, Numerical simulation of two experiments for studying propeller exciting forces, Ships Offshore Struc. 13 (2018) 1–8, https://doi.org/10.1080/17445302.2018.1430667.
[58] M. Cerny, C. Breitsamter, Investigation of small-scale propellers under non-axial inflow conditions, Aerosp. Sci. Technol. 106 (2020) 106048, https://doi.org/10.1016/j.ast.2020.106048, https://www.sciencedirect.com/science/article/pii/S1270963820307306.
[59] C. Paz, E. Suárez, C. Gil, J. Vence, Assessment of the methodology for the CFD simulation of the flight of a quadcopter UAV, J. Wind Eng. Ind. Aerodyn. 218 (2021) 104776.
[60] R.W. Deters, G.K.A. Krishnan, M.S. Selig, Reynolds number effects on the performance of small-scale propellers, in: 32nd AIAA Applied Aerodynamics Conference, 2014.
[61] M. Merchant, L. Miller, Propeller performance measurement for low Reynolds number UAV applications, https://doi.org/10.2514/6.2006-1127, 2006.
[62] K. Wang, Z. Zhou, X. Zhu, X. Xu, Aerodynamic design of multi-propeller/wing integration at low Reynolds numbers, Aerosp. Sci. Technol. 84 (2019) 1–17, https://doi.org/10.1016/j.ast.2018.07.023.
[63] O. Gur, A. Rosen, Propeller performance at low advance ratio, J. Aircr. 42 (2005) 435–441.
[64] S.-H. Peng, O. Grundestam, L. Tysell, Implementation and verification of computational aerodynamics for manoeuvring air vehicles, in: AIAA Aviation 2019 Forum, 2019.
[65] F. Menter, Two-equation eddy-viscosity turbulence models for engineering applications, AIAA J. 32 (8) (1994) 1598–1605, https://doi.org/10.2514/3.12149.
[66] F. Carneiro, L. Moura, P.C. Rocha, R.P. Lima, K. Ismail, Application and analysis of the moving mesh algorithm AMI in a small scale HAWT: validation with field test's results against the frozen rotor approach, Energy 171 (2019) 819–829, https://doi.org/10.1016/j.energy.2019.01.088.
[67] J. Brandt, M. Selig, Propeller performance data at low Reynolds numbers, in: 49th AIAA Aerospace Sciences Meeting Including the New Horizons Forum and Aerospace Exposition, 2011.
[68] C. Yonggang, W.H. Lam, H.T. Puay, M. Ibrahim, D. Robinson, G. Hamill, Component velocities and turbulence intensities within ship twin-propeller JET using CFD and ADV, J. Mar. Sci. Eng. 8 (2020) 1025, https://doi.org/10.3390/jmse8121025.
[69] T.-M. Propellers, T-motor store official, URL https://store.tmotor.com/.
[70] APC, Advanced APC propellers, URL https://www.apcprop.com/.
[71] K. Inagaki, F. Hamba, Modeling the energy flux enhanced in rotating inhomogeneous turbulence, in: Progress in Turbulence VIII, 2019, pp. 139–144.
[72] R.T.N. Chen, A survey of nonuniform inflow models for rotorcraft flight dynamics and control applications, in: NASA TM-102219, 1990.
[73] S. Houston, R. Brown, Rotor-wake modelling for simulation of helicopter flight mechanics in autorotation, J. Aircr. 40 (2003), https://doi.org/10.2514/2.6870.
[74] B. Theys, G. Dimitriadis, P. Hendrick, J. Schutter, Experimental and numerical study of micro-aerial-vehicle propeller performance in oblique flow, J. Aircr. 54 (2016) 1–9, https://doi.org/10.2514/1.C033618.